

# High-Fidelity numerical simulation of centrifuge tests on the superstructure-pile-liquefiable sand soil system

Degao Zou<sup>a,b</sup>, Tianju Wang<sup>a,b</sup>, Jingmao Liu<sup>a,b,\*</sup>, Kai Chen<sup>a,b</sup>, Bin Wang<sup>c</sup>,  
Xiuyang Zhang<sup>a,b</sup>

<sup>a</sup> The State Key Laboratory of Coastal and Offshore Engineering, Dalian University of Technology, Dalian, Liaoning, 116024, China

<sup>b</sup> School of Infrastructure Engineering, Dalian University of Technology, Dalian, Liaoning, 116024, China

<sup>c</sup> Powerchina Huadong Engineering Corporation Limited, Hangzhou, 311122, China

## ARTICLE INFO

### Keywords:

3D SBFEM-FEM  
State-dependent constitutive  
Liquefaction  
Superstructure-pile-soil interaction  
Seismic  
Deformation mode

## ABSTRACT

This study develops a three-dimensional (3D) cross-scale finite element simulation approach for the entire superstructure-pile-liquefiable sand system, based on the Scaled Boundary Finite Element Method and Finite Element Method (SBFEM-FEM) coupling analysis method for saturated porous media and incorporating a state-dependent generalized plasticity model. A high-fidelity numerical reproduction of centrifuge tests is conducted to validate the approach. First, the sand soil model parameters are calibrated based on existing research. Then, a cross-scale finite element analysis model is established, incorporating Goodman interface elements to simulate pile-soil interaction. The proposed method is validated through comparisons with experimental results, while the spatiotemporal distribution of excess pore water pressure (EPWP) in the soil is further analyzed to assess the effects of sand liquefaction on the pile and superstructure. The key findings are as follows: (1) The proposed method accurately captures the EPWP evolution and dynamic response of structures in sands with different relative densities; (2) A wedge-shaped pile-soil interaction zone exists at the mudline, where the soil first experiences dilation followed by contraction, resulting in significant oscillatory pore pressure. The pile within this zone bears a considerable horizontal load; (3) Three deformation modes of the pile foundation were identified. Liquefaction intensifies pile inclination in loose sand layers while reducing the horizontal displacement of the superstructure. The pile shaft embedded in the dense sand layer reduces the inclination, but the entire shaft embedded in the dense sand layer intensifies the dynamic response of the superstructure.

## 1. Introduction

In recent years, offshore wind power has seen rapid global growth, with an increasing number of countries leveraging it to meet energy demands. However, several offshore regions in Europe and the Asia-Pacific are located in high-seismic zones [1]. Seismic liquefaction is prevalent in these areas due to the widespread occurrence of fine sand and loose sandy soils [2–4], making them vulnerable to large-scale liquefaction during high-magnitude earthquakes. For instance, significant soil liquefaction was observed near the "Wind Power Kamisu" offshore wind turbines (OWTs) during the 9.0 Mw Tohoku earthquake in Japan in 2011 [5–7]. Furthermore, liquefiable soils have been linked to pile damage at numerous sites following strong earthquakes [8–11]. Therefore, the development of offshore wind farms must carefully

evaluate the impact of site liquefaction on structures caused by seismic loading [4].

The effective control of the dynamic response between the superstructure, pile foundation, and liquefied soil under seismic loading is a critical issue for researchers. The key challenge lies in understanding and predicting the influence of liquefied soil on pile foundation performance and its impact on the entire structural system. For horizontally loaded piles in sandy soils, the deformation criterion is more critical than the ultimate lateral bearing capacity, as excessive deformation may result in structural failure [12]. Therefore, evaluating the dynamic response of the superstructure, foundation, and liquefiable sands under seismic loads is crucial for ensuring the safety of the facility.

Researchers have used shaking table and centrifuge model tests to investigate the dynamic response characteristics of pile-liquefied sand

\* Corresponding author. The State Key Laboratory of Coastal and Offshore Engineering, Dalian University of Technology, Dalian, Liaoning, 116024, China.

E-mail addresses: [zoudegao@dlut.edu.cn](mailto:zoudegao@dlut.edu.cn) (D. Zou), [wangvn@mail.dlut.edu.cn](mailto:wangvn@mail.dlut.edu.cn) (T. Wang), [liujm@dlut.edu.cn](mailto:liujm@dlut.edu.cn) (J. Liu), [chenkai@dlut.edu.cn](mailto:chenkai@dlut.edu.cn) (K. Chen), [wang\\_b6@hdec.com](mailto:wang_b6@hdec.com) (B. Wang), [zhangxiuyang@mail.dlut.edu.cn](mailto:zhangxiuyang@mail.dlut.edu.cn) (X. Zhang).

<https://doi.org/10.1016/j.soildyn.2025.109565>

Received 25 February 2025; Received in revised form 22 April 2025; Accepted 1 June 2025

Available online 16 June 2025

0267-7261/© 2025 Elsevier Ltd. All rights reserved, including those for text and data mining, AI training, and similar technologies.

interactions. Wilson [13] systematically investigated the interaction mechanisms among superstructures, piles, and liquefied sand or clay through centrifuge shaking table tests. Bhattacharya et al. [14] revealed the detrimental effects of seismic-induced lateral spreading on pile bearing capacity and proposed a failure criterion based on the ratio of pile length to liquefaction depth. Yu et al. [15] compared the dynamic responses of gravity-based and monopile foundations for OWTs under liquefaction conditions, finding that gravity foundations exhibited significant settlement, while monopiles were more sensitive to lateral displacement. Wang et al. [16] through centrifuge tests on hybrid monopiles, found that the use of a friction wheel to apply additional confining pressure effectively suppressed soil liquefaction, resulting in significantly improved lateral stability compared to conventional monopiles. Dou et al. [17] using shaking table tests, demonstrated a stiffness enhancement effect of structures on liquefiable sites and quantified the positive impact of soil–structure interaction on seismic site stability. Xu et al. [18] conducted shaking table tests and numerical simulations under combined wind, wave, and earthquake loading. Preliminary results indicated that seismic loading dominated the structural dynamic response. While model tests offer direct observation opportunities, conducting full-scale experimental studies is often impractical due to challenges such as material preparation, high costs, and extended testing durations [19]. As a result, numerical simulation tools have gained increasing importance in analyzing liquefaction problems.

At present, two commonly used numerical simulation methods to describe seismic pile–soil interaction are  $p$ - $y$  curve method based on nonlinear Winkler foundation beam method (WFBM) [20–26] and numerical analysis method based on Biot porous media dynamics theory.

Most studies utilize the  $p$ - $y$  curve method based on WFBM for overall modeling of offshore wind turbine (OWT) systems. Brandenburg et al. [27] extended the  $p$ - $y$  method to liquefiable soils by applying a "p-multiplier". Liyanapathriana and Poulos [28]; Cubrinovski et al. [29]; Brandenburg et al. [30] introduced degraded soil stiffness into the  $p$ - $y$  equation. The soil resistance is reflected by a series of nonlinear springs on the pile using the ground motion and effective stress obtained from the free-field response analysis, but the near-field characteristics cannot be taken into account accurately. Mu et al. [31] integrated elastic foundation beam theory with the  $p$ - $y$  curve method to develop an analytical approach for single piles in sandy soil under complex loading conditions. Subsequently, a modified  $p$ - $y$  curve was derived based on the limit equilibrium theory [32]. Zhang et al. [33] integrated the theoretical model of shallow soil wedges with the theoretical model of flow failure around piles to modify the  $p$ - $y$  curves representing pile–soil interaction in saturated sandy foundations under varying degrees of weakening. However, the  $p$ - $y$  curves recommended by the American Petroleum Institute (API) exhibit excessive initial stiffness and underestimate foundation deformation. The  $p$ - $y$  curves of pile foundations are greatly influenced by pile diameter, ignores the continuity of the soil [34–36]. And it ignores the continuity of soil, failing to reveal the flow mechanism of surrounding soil around pile foundation under seismic action.

Several researchers adopted three-dimensional (3D) finite element method or 3D finite difference method for simulation, which properly considered the influence of motion and inertia interaction, as well as the influence of pore water pressure. Cheng and Jeremić [37] used 3D finite element modeling (FEM) to simulate the dynamic response of piles embedded in liquefied soils, emphasizing the importance of considering soil liquefaction in evaluating soil–structure interaction. Zhao et al. [38] observed that increasing the monopile diameter reduces the extent of soil liquefaction around the pile, and identified pile shaking as a primary cause of residual liquefaction near the pile foundation. Hussein and El Naggar [39] performed 3D FEM analyses of soil–pile–structure interaction in both liquefiable and non-liquefiable soils. Their results indicated that liquefaction leads to a reduction in lateral pile resistance as the thickness of the liquefied sand layer increases. In contrast, for non-liquefiable soils, the bearing capacity initially decreases and then

increases with pile diameter. Mo et al. [40] systematically investigated the effects of earthquake duration and velocity pulse on pile response in liquefied soils. Chen et al. [41] demonstrated that hybrid suction bucket foundations can significantly reduce the seismic response of OWTs and enhance the liquefaction resistance of the surrounding seabed. Cheng et al. [42] applied a 3D finite difference method to analyze the influence of earthquake magnitude and relative density on tripod suction bucket foundations, revealing their failure mechanisms in sandy soils.

Several studies have employed advanced constitutive models to analyze the liquefaction response of foundations [43–47]. Based on a deviatoric hardening plasticity model, Lü et al. [48] proposed a state-dependent model capable of predicting the onset of static liquefaction in unsaturated sandy soils containing gas bubbles. They later extended their research to investigate the static liquefaction behavior of sand mixtures [49]. Liu et al. [50] evaluated the effects of pile diameter, relative density, and embedment depth on the lateral response of piles in two types of sandy soils using the hypoplastic constitutive model. Zhang et al. [51] employed the PIMY02 constitutive model to evaluate the reinforcement effectiveness of concrete and gravel piles in sloping liquefiable ground. The results indicated that, under the same embedment depth and pile diameter, concrete piles exhibited superior reinforcement performance compared to gravel piles.

Additionally, some studies have adopted a rigid beam-column connection between pile beam elements and surrounding soil elements to physically represent the pile cross-section [52–55]. However, Wotherspoon [56] and Sánchez and Roesset [57] report that since beam elements do not reflect the geometric cross section of the pile, this approach tends to underestimate the stiffness of the pile. Bao et al. [45] by comparing the numerical analyses of different pile foundation elements types, concluded that the pile volume needs to be taken into account regardless of whether it is a small or a strong ground vibration. Therefore, it is necessary to build a complete 3D model of the superstructure-pile-liquefiable sand system in the finite element mesh, so as to provide a more realistic physical characterization of the pile–soil system. However, the 3D nonlinear finite element analysis method (FEM) is time-consuming and the constitutive model involves a complex hardening law, which leads to a relatively low computational efficiency in saturated porous media.

In offshore wind power projects, a refined and rapid analysis method is urgently needed for the dynamic response of superstructure-pile foundation-liquefiable sand. In this paper, a 3D finite element analysis method for monopiles in liquefiable sands is developed based on the state-dependent generalized plasticity model [58] with the SBFEM-FEM (Scaled Boundary Finite Element Method and Finite Element Method) coupled analysis method for saturated porous media [59–61]. Firstly, a cross-scale refinement analysis model of superstructure-pile-liquefiable sand was established in GEODYNA [62], and the model parameters were strictly calibrated based on Nevada sand triaxial test. Secondly, the accuracy and efficiency of the present method is verified by comparing different finite element meshes with the existing centrifugal test results. In addition, the spatial and temporal distribution pattern of excess pore water pressure (EPWP) around the pile and the effect of liquefied sands on the dynamic response of the system are explained. The proposed method balances computational efficiency and accuracy, increasing computation speed by 40 %. It overcomes limitations of API-based  $p$ - $y$  curves for modeling complex dynamic responses under liquefaction. Three pile deformation modes in liquefied soil layers were identified, supporting large-scale offshore wind turbines (OWTs) system analysis.

## 2. Three-dimensional finite element analysis

Using a state-dependent generalized plasticity constitutive model, we establish a time-domain numerical method. The model parameters were first calibrated, followed by a cross-scale refined analytical model of superstructure-pile-liquefiable sands. In comparison with the centrifugal test, the method's applicability was verified.

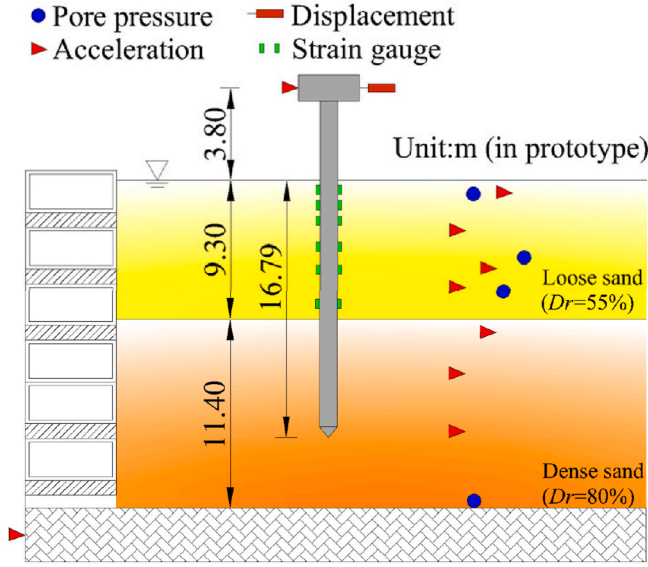


Fig. 1. Centrifuge test CSP3.

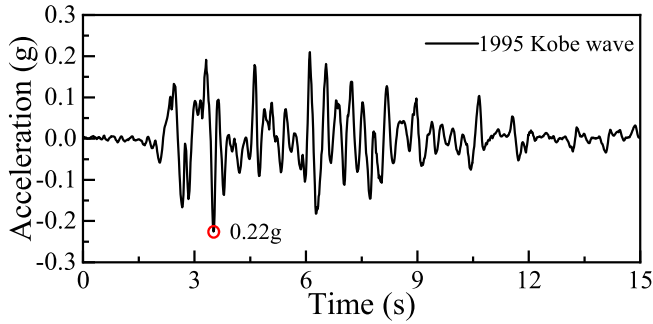


Fig. 2. Acceleration time history for the Kobe (1995) wave.

### 2.1. Centrifuge test description

Wilson [13] highlighted that the widespread pile foundation damage observed during the 1995 Kobe earthquake clearly demonstrated the potential severity of liquefaction-induced failures. Method validation was carried out using the CSP3 centrifugal test recorded by Wilson, in which a monopile was buried in two layers of saturated, uniformly graded Nevada sand and subjected to a 30g centrifugal test. As shown in Fig. 1, the centrifugal test arrangement on a prototype scale consists of an upper layer of liquefiable loose sand with a relative density ( $D_r$ ) of 55 % and a lower layer of non-liquefiable dense sand with a density ( $D_r$ ) of 80 %. The pile wall thickness is 0.019m, and the pile foundation outer

diameter ( $D$ ) is 0.67m. The superstructure has a mass of 480 KN and is 3.8 m above the ground. Ground motion input was based on the time history data of the 1995 Kobe earthquake (see Fig. 2), and the peak acceleration was 0.22g. As shown in Fig. 3, the bedrock-type ground motion of the Kobe earthquake, characterized by high-frequency dominance, exhibits significant destructive effects on short-period pile foundations. Table 1 counts the pile-soil interaction (PSI) calculation methods and validation contents used by some researchers to numerically simulate the CSP3 centrifugal test. As mentioned earlier, some researchers used Winkler models to simulate PSI [13,21–23,28] and others used the rigid beam-column elements method [52,54]. Comparing to the centrifugal test, the researchers gave the simulation results of some of the test data for single or multiple points.

### 2.2. Program overview and core features

Numerical simulations were carried out using the geotechnical finite element software GEODYNA, which has been widely used in seismic design applications for earth and rock dams, nuclear power plants, and breakwaters [63–69]. The core features of the program are summarized as follows:

- (1) Versatile modeling capabilities: Developed using Visual Studio C++ and the MFC environment, the software adopts object-oriented design principles such as abstraction, inheritance, overloading, and polymorphism. It encapsulates key components of finite element analysis—including constitutive models, pore water seepage models, seismic pore pressure models, element types, load types, and solvers—into a robust geotechnical analysis framework. In this study, both FEM and SBFEM elements are used with seismic wave input applied as dynamic loading and solved iteratively.
- (2) Unified analysis framework: The software integrates a wide range of models established through previous research on seismic failure of large-scale geotechnical structures, including the generalized plasticity model for rockfill, the plastic-damage model for concrete, the 3D elasto-plastic contact model, and seismic wave input methods. In this work, the generalized plasticity model is used to simulate pile failure in liquefiable sands.
- (3) Refined analysis methods: A super element (S-element) data structure is developed using object-oriented C++ to integrate polygonal/polyhedral SBFEM, meshfree interface simulation techniques, and conventional FEM within a unified framework. The super element class allows direct access to GEODYNA's extensive material, loading, and algorithm libraries, enabling seamless coupling of SBFEM-FEM-MFM for refined multiscale analysis. Moreover, the use of dynamic-link libraries facilitates coupling with discrete element and material point methods, offering an effective solution for large-deformation and failure analysis in geotechnical engineering.

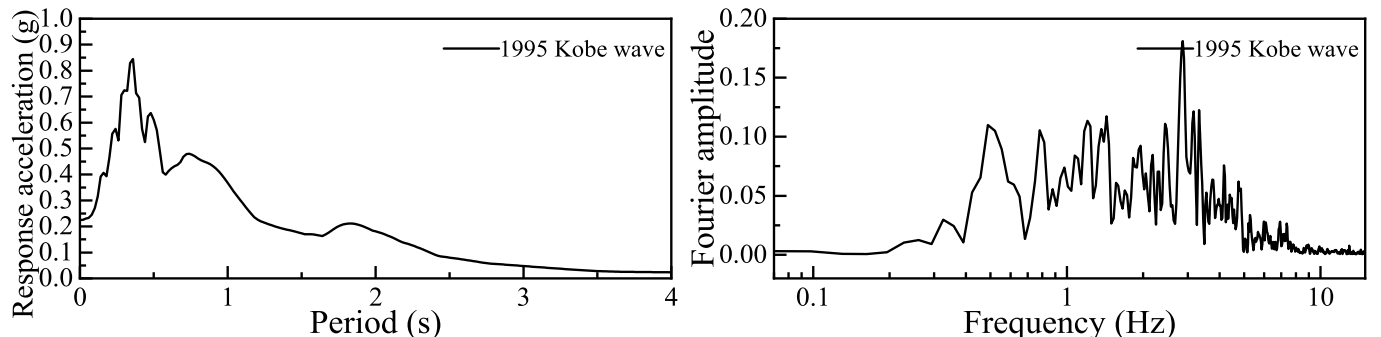
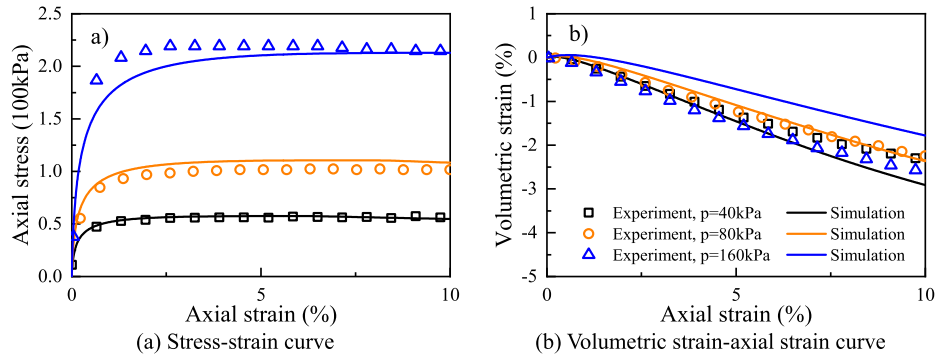


Fig. 3. Acceleration response spectrum and Fourier spectrum.

**Table 1**  
CSP3 centrifuge test numerical simulation statistics.

Researcher	PSI-research method	Monitoring point	Pile- element type	Verify content				
				Soil Acc.	Soil Epwp.	Pile Dis.	Structure Acc.	Structure Dis.
Wilson (1998) [13]	Winkler models	Multiple points	6061Al beam	✓	✓	✓	✓	✓
Liyanapathirana and Poulos (2005) [28]	Winkler models	single-point	beam	–	✓	✓	✓	–
Rahmani and Pak (2012) [52]	rigid beam-column elements	Multiple points	beam	–	✓	–	✓	–
Janalizadeh and Zahmatkesh (2015) [21]	Winkler models	single-point	beam	–	–	✓	–	✓
Wang et al. (2019) [22]	Winkler models	Multiple points	beam	✓	✓	✓	✓	✓
Patra and Haldar (2021) [23]	Winkler models	single-point	beam	–	✓	–	✓	✓
Abbasi et al. (2023) [54]	rigid beam-column elements	Multiple points	beam	✓	✓	–	✓	✓
This study	interface element	Multiple points	solid	✓	✓	✓	✓	✓



**Fig. 4.** Simulation of three drained constant- $p$  tests on Nevada sand with  $Dr = 40\%$ .

Details of the centrifuge model setup, boundary conditions, pile–soil interaction, and damping are described in Section 2.4.

### 2.3. Constitutive model and parameter calibration

The software design and development of the program are based on the Biot consolidation theory, which utilizes the Biot dynamic consolidation equations in  $u$ - $p$  form to discretize the spatial domain. Additionally, it introduces the matrix form of Rayleigh damping in the following equation:

$$\mathbf{M}\ddot{\mathbf{u}} + \mathbf{C}\dot{\mathbf{u}} + \mathbf{K}\mathbf{u} - \mathbf{Q}\bar{\mathbf{p}} - \mathbf{f}_u = \mathbf{0} \quad (1)$$

$$\mathbf{M}_f\ddot{\mathbf{u}} + \mathbf{Q}^T\dot{\mathbf{u}} + \mathbf{S}\bar{\mathbf{p}} + \mathbf{H}\bar{\mathbf{p}} - \mathbf{f}_p = \mathbf{0} \quad (2)$$

Where  $\mathbf{M}$  is the mass matrix of the soil;  $\mathbf{C}$  is the damping matrix;  $\mathbf{Q}$  is the coupling matrix;  $\mathbf{f}_u$  is the load vector of the soil;  $\mathbf{M}_f$  is the mass matrix of the fluid;  $\mathbf{S}$  is the compression matrix of the fluid;  $\mathbf{H}$  is the permeability matrix of the fluid;  $\mathbf{f}_p$  is the load vector of the fluid;  $\ddot{\mathbf{u}}$ ,  $\dot{\mathbf{u}}$  and  $\mathbf{u}$  are the nodal acceleration, velocity, and displacement vectors, respectively;  $\bar{\mathbf{p}}$  and  $\dot{\bar{\mathbf{p}}}$  are the nodal pore pressures and their first-order derivatives, respectively. The dynamic governing equations of saturated soils are discretized in the time domain using the generalized Newmark method.

The state-dependent generalized plastic constitutive model proposed by Liu et al. [58] is employed in this study to simulate the nonlinear behavior of sands. The model is based on the Wang et al. [70] and Li [71] frameworks. The model introduces the advantages of proportional memory model theory [72], critical state theory and boundary surface theory, etc. The improved model can better describe the 3D complex deformation characteristics of sand and characterize the stress-strain response of sand with different relative densities through a set of material parameters. For the specific modelling framework and model

implementation see Liu et al. [58].

The above model was used to calibrate the model parameters of Nevada No 120 sands, which is the special sand of Earth Technology Corporation in VELACS project. The tests were conducted with average initial perimeter pressures ranging from 40 kPa to 160 kPa, while the relative densities of the prepared sandy soils varied between 40 percent and 60 percent, as elaborated by Arulmoli et al. [73].

In Figs. 4 and 5, the monotonic compression tests for sandy soil drainage with  $Dr = 40\%$  and  $60\%$  are compared with numerical simulation results. Furthermore, Fig. 6 presents the response of excess pore water pressure (EPWP), shear response, and stress paths in the undrained cyclic triaxial test for sandy soils with  $Dr = 40\%$ . The findings demonstrate that the proposed constitutive model effectively captures the stress-strain behavior of sandy soils with varying relative densities, while also depicting the gradual development of EPWP. The calibrated parameters of Nevada sandy soil, obtained through numerical simulation of triaxial tests, are presented in Table 2.

### 2.4. Three-dimensional (3D) finite element model

As illustrated in Fig. 7, a cross-scale refined analysis model of superstructure-pile-liquefiable sands was developed based on the centrifugal experiments in Section 2.1 above. Table 5 presents the statistics of the elements for each component in the model.

**Soil:** The material properties of the Nevada sand utilized in the numerical model are presented in Table 3. The soil range is  $46\text{m} \times 16\text{m} \times 20.7\text{m}$ , and there are 20,536 elements. In order to improve the computational efficiency and ensure the computational accuracy, combined with the Scaled boundary finite element method and finite element method (SBFEM-FEM) coupling analysis method of saturated porous media, octree discretization technique was used for cross-scale modeling [67,68,74]. The scaled boundary finite element method



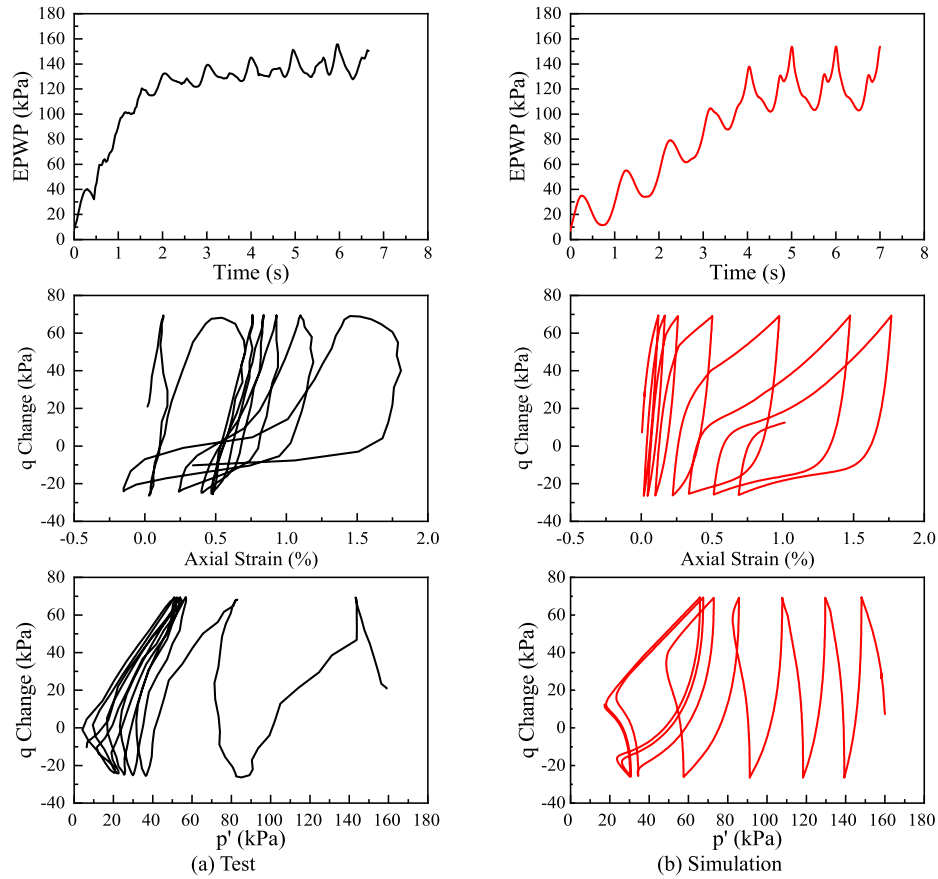


Fig. 5. Simulation of three drained constant- $p$  tests on Nevada sand with  $Dr = 60\%$ .

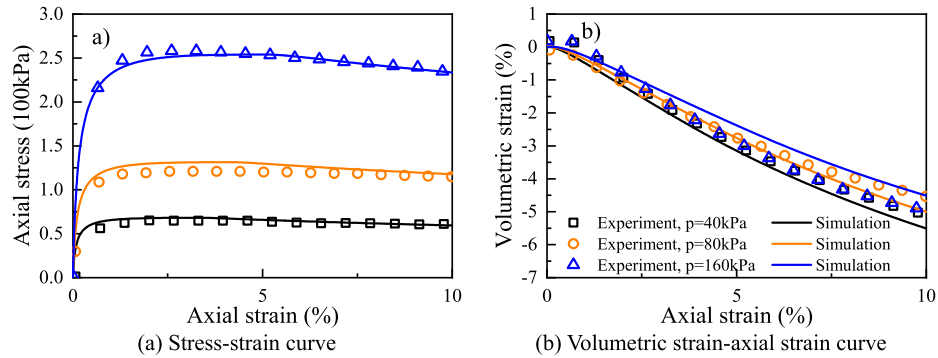


Fig. 6. Simulation in undrained cyclic triaxial tests on Nevada sand with  $Dr \approx 40\%$ .

Table 2

Simulation parameters for Nevada sand.

Elasticity			Critical state			State dependent parameter			Dilatancy drij-mechanics		Dilatancy dp'-mechanics						
$G_0$	$\nu$	$Em$	$Mc$	$\lambda$	$e_{r0}$	$\beta$	$n_g$	$n_b$	$\alpha_1$	$r_l$		$h_2$	$m_p$	$h_3$	$\alpha_2$	$\alpha_3$	$c_0$
150	0.1	0.5	1.14	0.022	0.809	0.4	2.5	4.5	0.6	1.0		10	0.5	10	1.5	1.0	0.5

(SBFEM) is a semi-analytical, high-precision numerical approach that discretizes the circumferential direction while solving analytically in the radial direction [75,76]. By integrating the advantages of the finite element method (FEM) and the boundary element method (BEM), SBFEM overcomes their respective limitations, making it well-suited for solving problems involving finite domains, infinite domains, multiscale interactions, and fracture mechanics [77]. For instance, in OWTs foundation studies, the computational domain scales of pile foundations and

the surrounding soil can differ by two orders of magnitude. SBFEM enables efficient multiscale analysis in such cases. In this study, high-precision SBFEM is employed for the transition elements [78,79], as shown in Fig. 7, where each transition element consists of nine faces and thirteen nodes. This approach effectively mitigates the computational inefficiency associated with conventional fine-scale uniform meshing. As shown in Table 5, traditional elements constitute 99.14 % of the model, while transitional elements account for 0.86 % of the model.

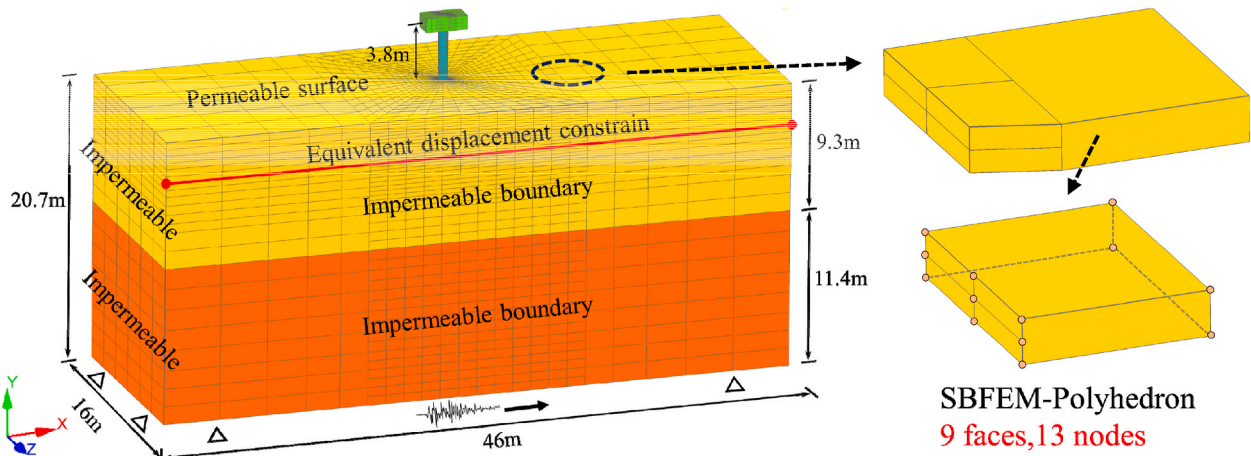


Fig. 7. Three-dimension finite element model.

**Table 3**  
Physical properties of Nevada sand.

Parameter	$D_r$	Porosity	Void ratio	Saturated unit weight	Permeability
Unit				$\text{kN/m}^3$	$\text{m/s}$
Value	55 %	0.409	0.730	19.87	$6.05 \times 10^{-5}$
	80 %	0.377	0.606	20.41	$3.70 \times 10^{-5}$

**Table 4**  
Interface element parameters.

$k_1$	$k_2(\text{kPa/m})$	$n$	$\varphi$
800	$1 \times 10^7$	0.5	27

**Table 5**  
Statistics of the element types in the core wall model with an octree mesh.

Element types	Faces in one element	Part	Number	Percentage (%)	Sum (%)
Conventional element	6	Sandy Soil	20032	65.60	99.14
	6	Pile	7040	23.06	
	6	Superstructure	1216	3.98	
	6	Interface	1984	6.50	
Polyhedron	9	Sandy Soil	264	0.86	0.86

This type of polyhedral transition element serves as a critical bridge connecting coarse and fine meshes, and is an essential prerequisite for enabling efficient cross-scale analysis.

**Pile:** The pile used in the numerical modelling are considered to be impermeable linear elastic materials. The pile was constructed with a Young's modulus of 210 GPa, a density of  $7800 \text{ kg/m}^3$  and Poisson's ratio of 0.3. Eight node-hexahedral elements were used to disperse the pile and superstructure, with a total of 8256 elements. The results are not easy to converge due to the large difference between the stiffness of the pile and the soil, the small size of the pile wall will significantly reduce the efficiency of the calculation, so the pile foundation is modelled as an equivalent solid pile using an equivalent conversion of stiffness and density, as shown in Refs. [80–82]. In the equivalent solid pile, the length and outside diameter of the pile are kept unchanged, the equivalent Young's modulus  $E_{sp}$  and density  $\rho_{sp}$  are calculated to ensure the total mass and bending stiffness remains unchanged. Both can be determined by the following equation,

**Table 6**  
Numerical simulation working cases.

Working cases	Case description	Grid density	Mesh type	Depth of liquefiable sands	$D_r$
1	In order to compare the applicability and superiority of the method	Mesh A	FEM	9.3m	55 %
2		Mesh B	SBFEM + FEM	9.3m	80 %
3		Mesh C	FEM	9.3m	55 %
4	To investigate the effect of liquefaction on the dynamic response of the system	Mesh B	SBFEM + FEM	0.0m	80 %
5		Mesh B	SBFEM + FEM	20.7m	55 %

$$E_{sp} \frac{\pi D^4}{64} = E_{hp} \frac{\pi (D^4 - d^4)}{64} - E_s \frac{\pi d^4}{64} \quad (3)$$

$$\rho_{sp} A_{sp} = \rho_{hp} A_{hp} + \rho_s (A_{sp} - A_s) \quad (4)$$

A hollow pile has an elastic modulus, density, and cross-sectional area of  $E_{hp}$ ,  $\rho_{hp}$ , and  $A_{hp}$ , respectively. A solid pile has an elastic modulus, density, and cross-sectional area of  $E_{sp}$ ,  $\rho_{sp}$ , and  $A_{sp}$ . A diameter and an inner diameter of  $D$ ,  $d$  respectively;  $E_s$  is the average elastic modulus of the sand in the middle of the embedded depth of the pile.  $\rho_s$  is the sand density. Based on the above equivalent conversion, the density and Young's elastic modulus of the solid pile section are  $300 \text{ kg/m}^3$  and  $14.6 \text{ GPa}$ , respectively.

**Pile-Soil interface:** Goodman interface element is used for pile-soil interaction [63]. Zhang et al. [83] calibrated this interface element parameters based on Said et al. [84]'s research, and successfully applied it to a large diameter monopile foundation model in sands. The final parameters are listed in Table 4.

**Boundary conditions:** To simulate the undrained behavior of sands during an earthquake, impermeable boundaries are applied at the bottom and sides, with a permeable top boundary. The bottom boundary is fully constrained in all directions. For the side boundaries, an equivalent

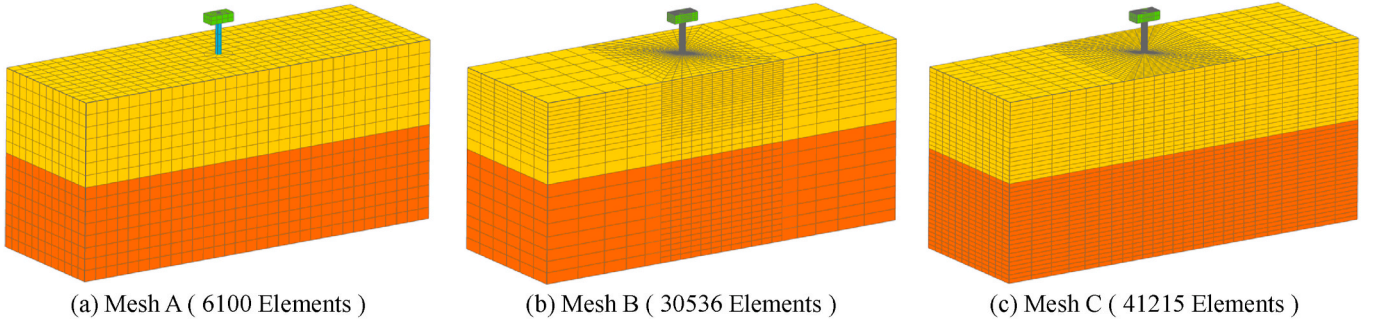


Fig. 8. Three-dimensional numerical model with different mesh density.

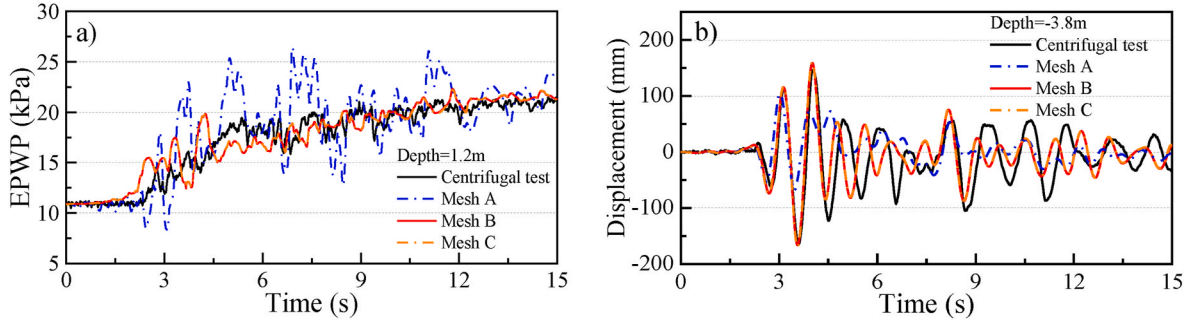


Fig. 9. Calculation results of different mesh densities: (a) EPWP time history; (b) Time history of horizontal displacement of superstructure.

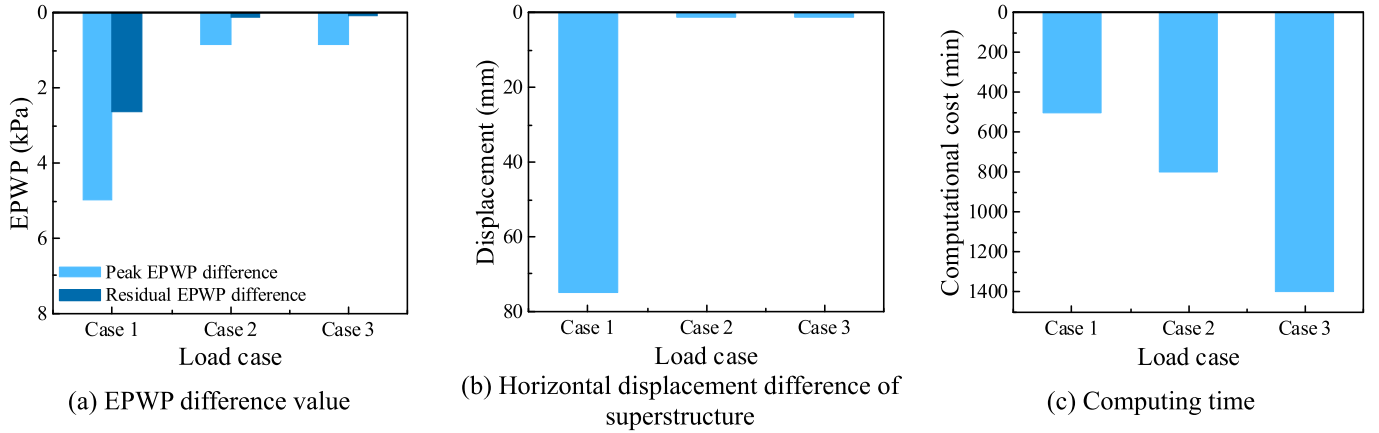


Fig. 10. Comparison of calculation accuracy and efficiency of different mesh density.

displacement constraint is implemented to simulate seismic wave propagation in the X-direction. This ensures that nodes at the same elevation on both sides of the model undergo identical displacements, preventing the reflection of seismic waves.

**Damping:** According to Wilson [13], 5 % damping ratio was recommended for soil under seismic loads. The superstructure and pile foundation are damped at 1 %.

**step:** In the initial stage of analysis, gravity is applied to the liquefiable soil to establish an initial stress balance. The second step is to install the pile foundation and superstructure in the center of the soil domain, remove the corresponding soil mass, and apply gravity to balance the soil stress field twice. The third step applies the X-direction seismic acceleration at the bottom.

### 3. Method verification

#### 3.1. Mesh verification

Firstly, the feasibility of the coupled SBFEM-FEM analysis method is explored by comparing it with finite element methods with different mesh sparsity levels. Secondly, the influence of the liquefaction soil layer on the dynamic response of the whole system was discussed. All cases are recorded in Table 6.

To further demonstrate the superiority of the present methodology, the above models in this study were compared with grids with different degrees of density, as shown in Fig. 8(a), (b) and (c), whose sizes were consistent with those described above. Fig. 8(a)–(c) are the FEM model, and Fig. 8(b) are the coupling analysis model of SBFEM-FEM.

Fig. 9 shows the calculation results of EPWP and superstructure displacement for three different mesh densities. The results show that when finite element analysis model is used, the sparse mesh (Case 1) will

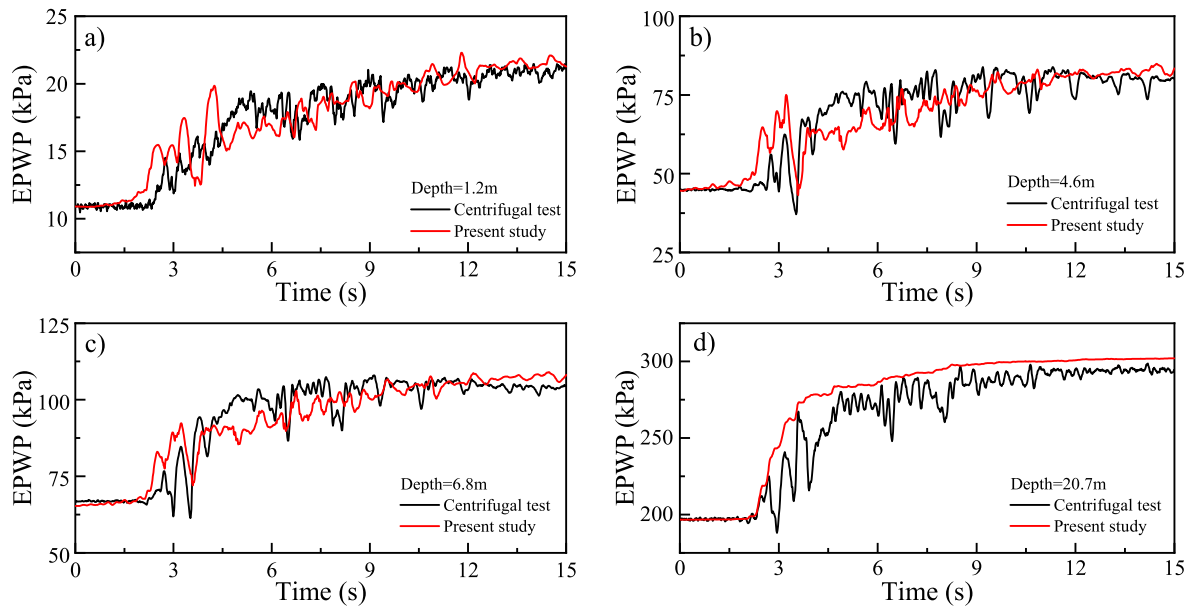


Fig. 11. Comparison of the pore water pressure time history at different depth: (a) Depth = 1m; (b) Depth = 5m; (c) Depth = 7m; (d) Depth = 21m.

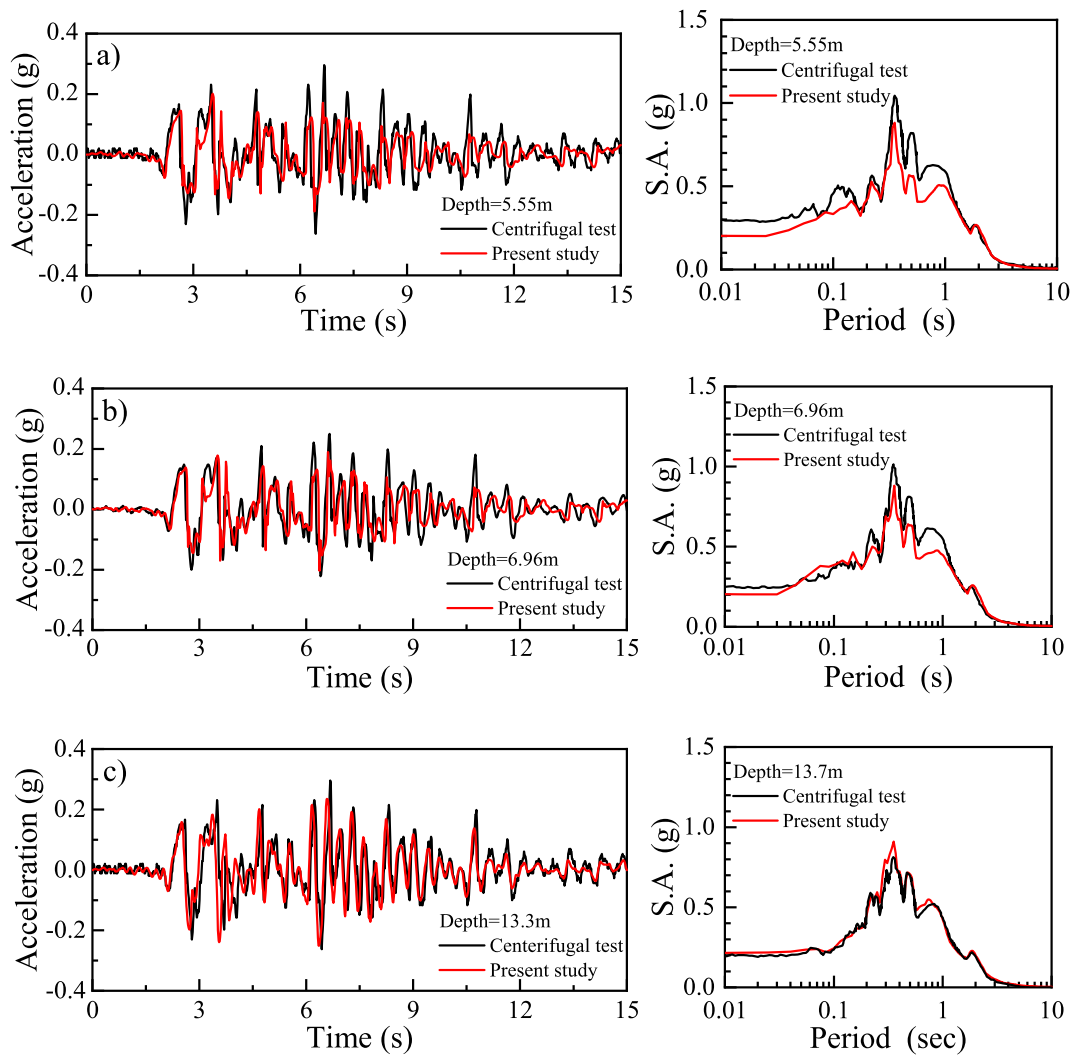


Fig. 12. Comparison of acceleration time histories of soil accelerations and associated spectra (5 % damping) at different depth: (a) Depth = 6m; (b) Depth = 7m; (c) Depth = 14m.



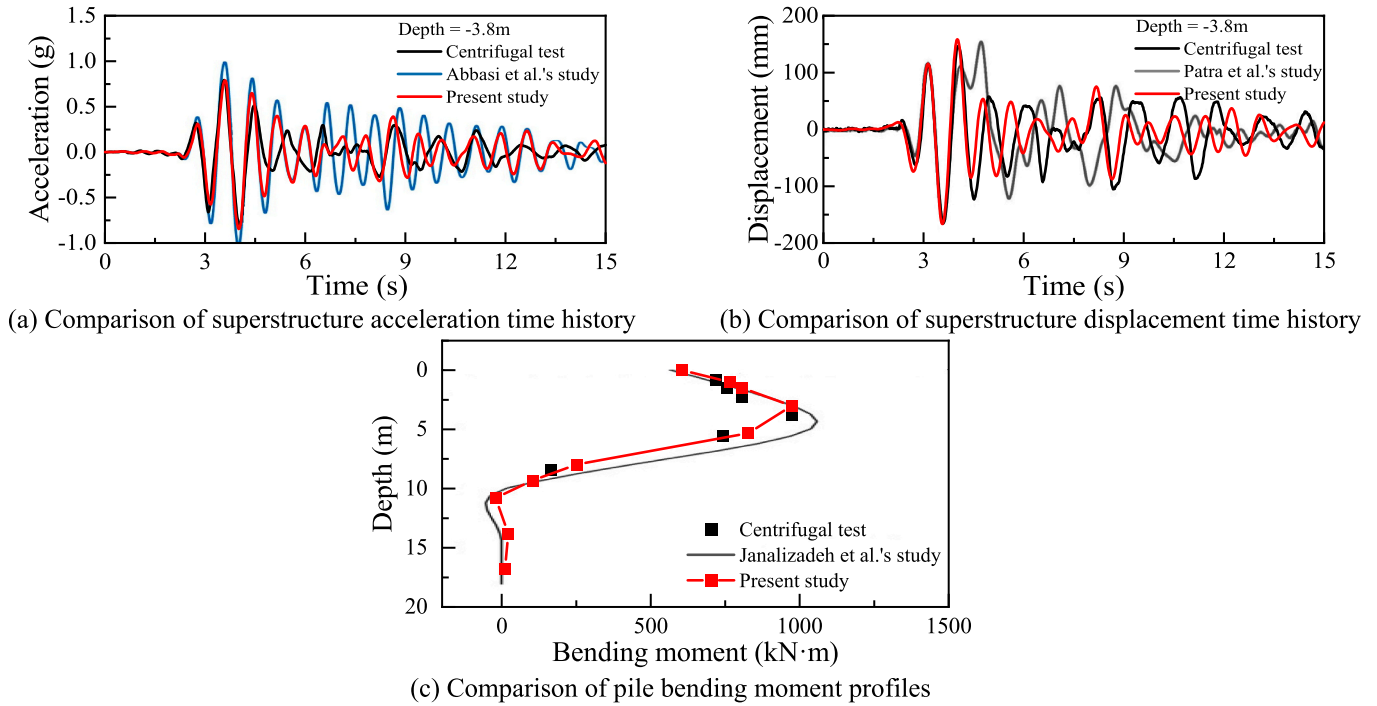


Fig. 13. Comparison of dynamic response results of superstructure and pile.

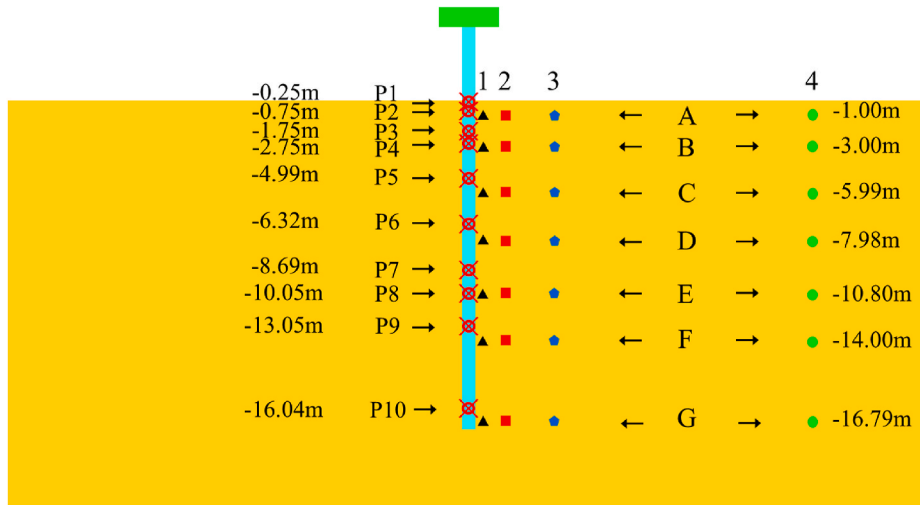


Fig. 14. Layout of monitoring points.

Table 7

Location and intention of monitoring points.

Monitoring points	Locations	Intention
A1-G1	Range = 0.63m ( $\approx 0.9$ Diameter)	Investigate the spatiotemporal distribution pattern of pore pressure
A2-G2	Range = 2.04m ( $\approx 3.0D$ )	
A3-G3	Range = 4.81m ( $\approx 7.1D$ )	
A4-G4	Range = 18.88m ( $\approx 28.2D$ )	
P1-P10	In pile foundation	Investigate the interaction mechanism between piles and soil

lead to larger oscillation of EPWP calculation, smaller peak horizontal displacement of superstructure, inaccurate calculation results. From Fig. 10, it is observed that in the high-density mesh scenario (Case 3), although the computed results closely match the experimental data, the computation time reaches 1400 min, making it impractical for large-scale simulations. In contrast, the coupled analysis model (Case 2) achieves pore pressure and displacement responses with deviations of less than 1 % compared to experimental results, while improving computational efficiency by 40 %. Therefore, employing this approach and encrypting the cells around the pile not only ensures precise calculations but also enhances computational efficiency, thereby facilitating large-scale offshore wind power computations in subsequent analyses.

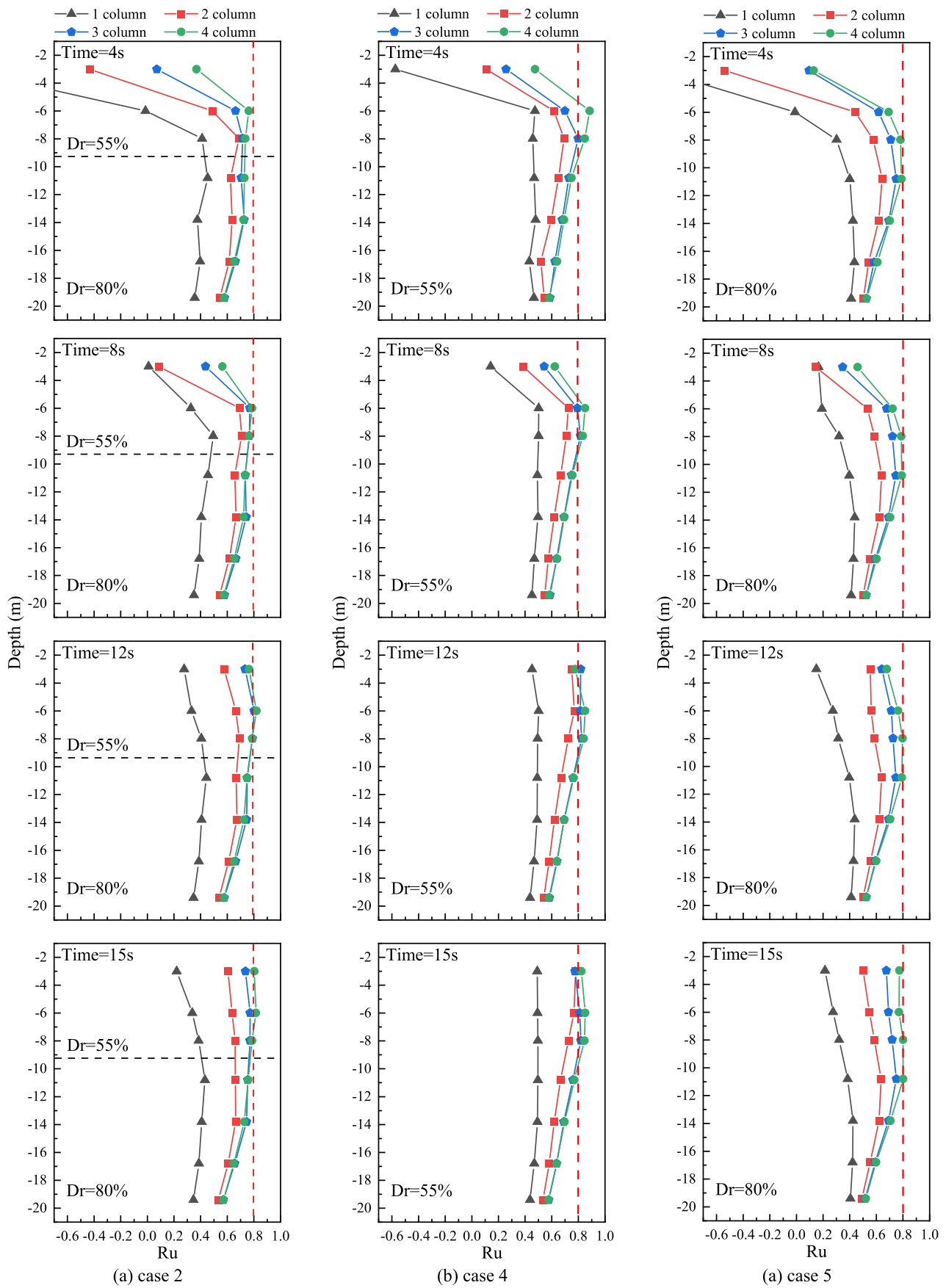


Fig. 15. Ru profiles at different monitoring points and time points for the three cases.

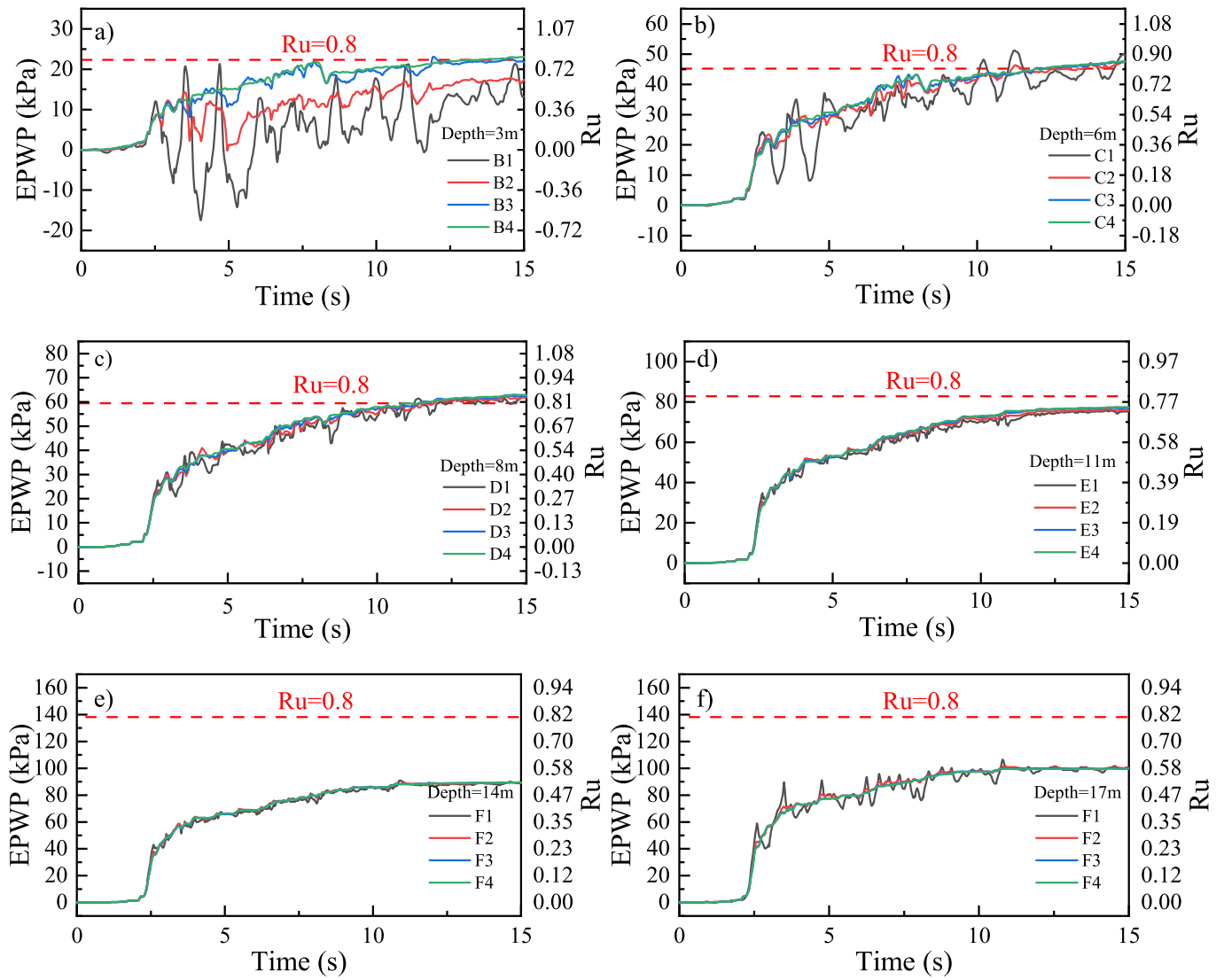


Fig. 16. Time history of EPWP development at different positions in Case 4: (a) Depth = 3m; (b) Depth = 6m; (c) Depth = 8m; (d) Depth = 11m; (e) Depth = 14m; (f) Depth = 17m.

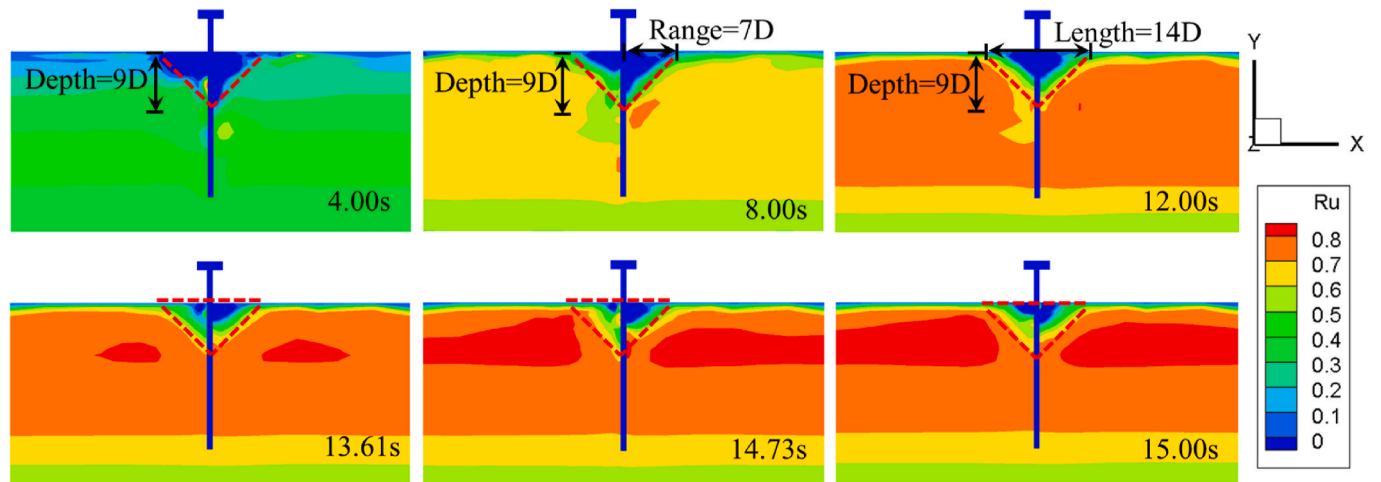


Fig. 17.  $R_u$  development time cloud diagram for Case 2.

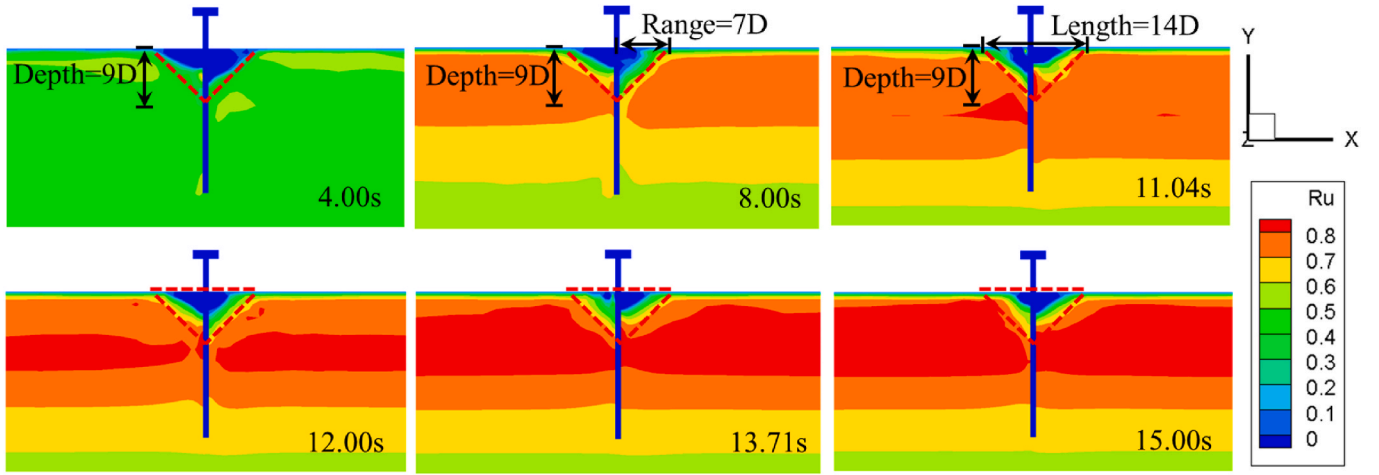


Fig. 18. Ru development time cloud diagram for Case 4.

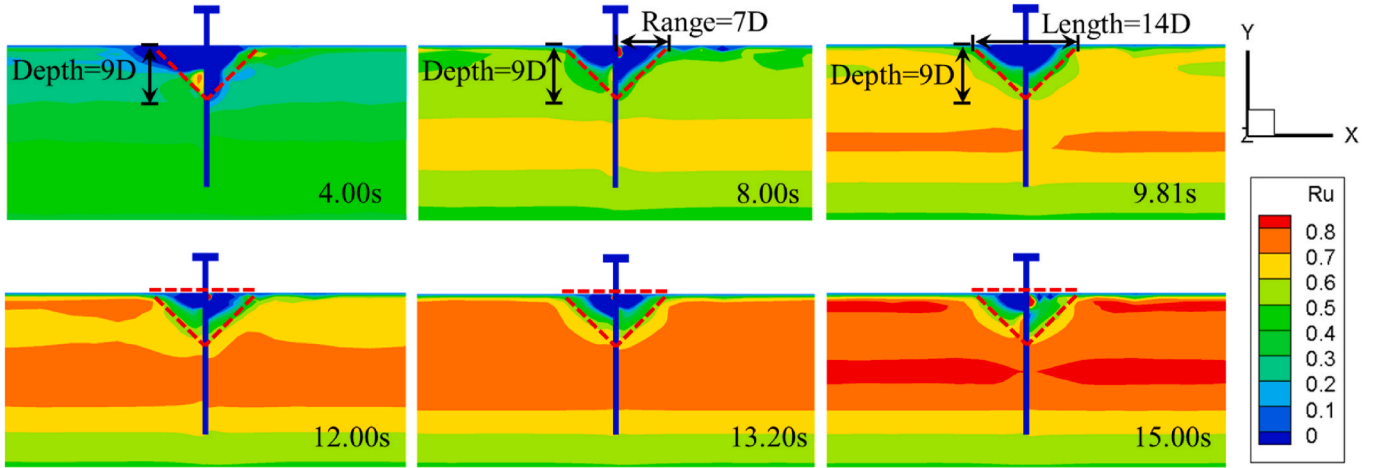


Fig. 19. Ru development time cloud diagram for Case 5.

### 3.2. Result verification

Fig. 11 compares the simulated and experimental pore water pressure time histories at different soil depths. Fig. 12 presents the acceleration response time histories of soil layers at depths of 5.55 m, 6.96 m, and 13.3 m. The numerical results exhibit good agreement with experimental data, effectively capturing the pore pressure and acceleration responses of soil layers with different relative densities under pile-soil interaction. Fig. 13 compares the analysis results of the FEM and  $p$ - $y$  curve methods for the CSP3 centrifuge test from existing studies. By comparing the dynamic response time history of the superstructure and the moment envelope of the pile, the peak responses obtained in this study deviate from the experimental results by less than 5 %, demonstrating good overall agreement. These findings validate the reliability of the proposed numerical simulation method in predicting pile-soil interaction, pore pressure evolution, and system dynamic response.

## 4. Results and discussion

This section provides a detailed analysis of the spatial and temporal variations in liquefaction distribution during dynamic response, highlighting the liquefaction development patterns. The study investigates the horizontal displacement, acceleration, rotation, and horizontal interaction responses between the pile and surrounding soil, elucidating the influence domain of pile-soil interactions and the impact of sand

liquefaction on the system.

### 4.1. EPWP response

The development of dynamic pore pressure is the key to using effective stress method to analyze the dynamic stability of soil in the liquefiable sandy seabed with pile-soil interaction. Additionally, it is a significant factor influencing soil deformation and strength under seismic loading. In this paper, the excess pore water pressure ratio (Ru) is defined as the ratio of excess pore water pressure to initial vertical effective stress [85],  $Ru = \Delta u / \sigma'_{v0}$ , where  $\Delta u$  is the difference between the current EPWP and the hydrostatic pressure,  $\sigma'_{v0}$  is the initial vertical effective stress. The region with  $Ru \geq 0.8$  at the end of the earthquake is regarded as a liquefaction region [86].

Fig. 14 presents the layout diagram of the monitoring points for this study. To investigate the influence range of pile-soil interaction and the seismic response characteristics of the soil foundation and pile, a series of monitoring points are arranged within the 3D numerical model. These monitoring points are normalized by the pile diameter  $D$  ( $D = 0.67$  m) to examine the variations in excess pore water pressure (EPWP) and acceleration along both horizontal and vertical directions at various locations, as well as changes in the horizontal displacement of the pile body. For details about the locations of monitoring points, see Table 7.

Fig. 15 shows the spatial and temporal distribution curves of Ru for three cases (Time = 4s, 8s, 12s, 15s). From Fig. 15, it can be clearly seen



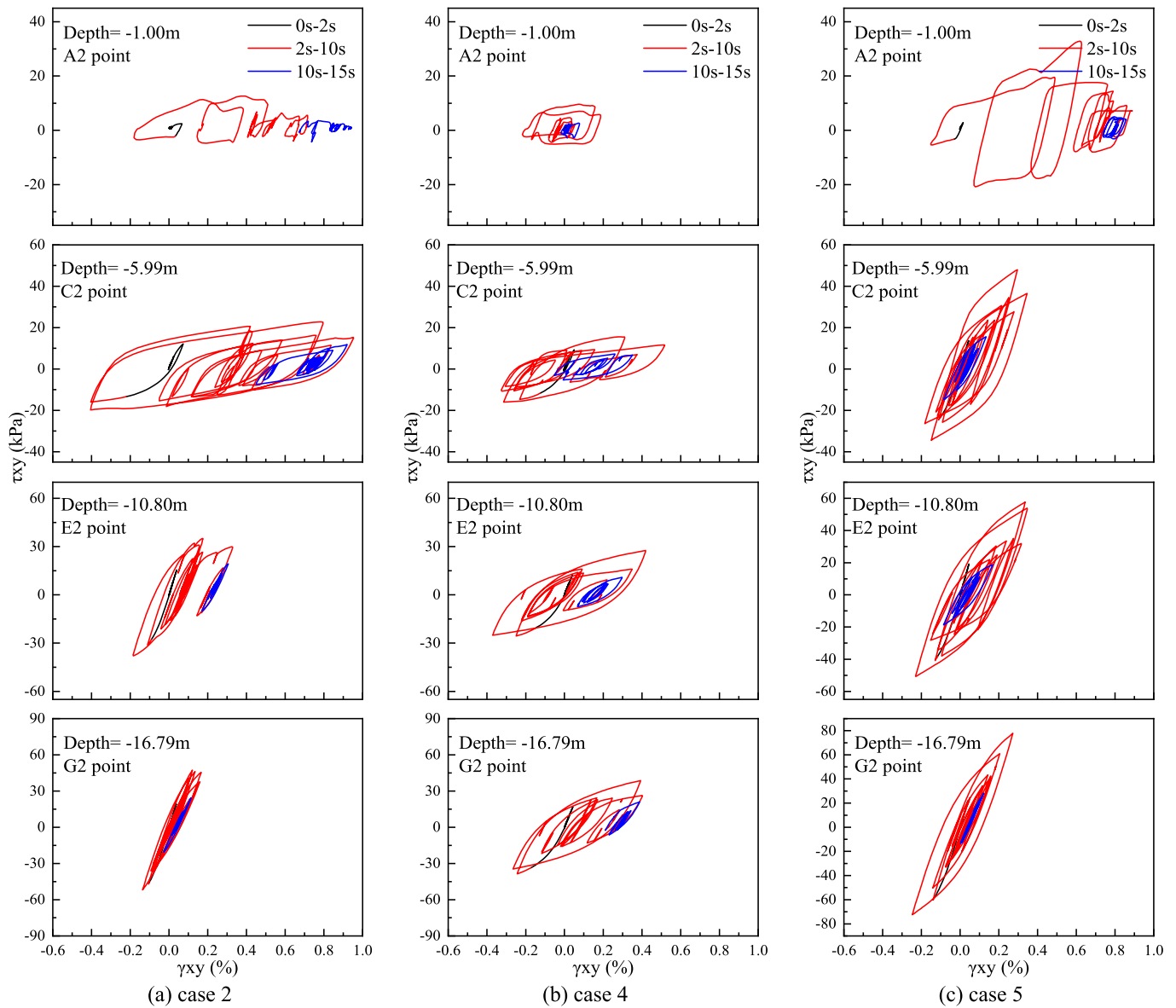


Fig. 20. Stress-strain curves of the soil around the pile for three cases.

that within 8s for all cases at the same depth horizontally, the Far-pile column 4 (Range  $\approx 28D$ ) has the largest  $R_u$  value, and the trend for column 3 (Range  $\approx 7D$ ) is within 5 % of it; At -6m (Depth  $\approx 9D$ ) in the same range depth direction, the  $R_u$  varies significantly. This indicates that the pile-soil interaction affects the pore pressure within  $7D$  horizontally (i.e.  $14D$  at the center of the pile) and within  $9D$  of the soil surface. The smaller  $R_u$  values in column 1 and column 2 indicate that the pile foundation improves the liquefaction resistance of the surrounding soil. Pore pressure development could see Figs. 17–19.

In Fig. 15, significant "negative pore pressure" occurs in the shallow soil within a radius of approximately  $3D$  from the pile center, followed by a subsequent accumulation of positive pore pressure. This phenomenon is due to pile-soil interactions, which cause the surrounding sand to undergo dilation followed by contraction within the influence domain of the pile, resulting in an instantaneous seepage force. Comparing Fig. 15 (b) and (c), the trend of  $R_u$  with depth is similar in both loose and dense sand; however, at all depths, the loose sand exhibits higher  $R_u$  values and a broader liquefaction range. In Fig. 15(a), the upper and lower layers of soil also follow the same pattern as above.

Taking case 4 as an example, Fig. 16 shows the evolution of EPWP with time at each measurement point under seismic loading.

Observations show that the changes in EPWP during the earthquake can be clearly divided into three phased characteristics (Post-earthquake consolidation and pore pressure dissipation were not accounted for in the analysis). In the initial phase 0s–2.5s, the accumulation of EPWP is slow due to the small ground shaking acceleration. The second stage 2.5s–10s, the EPWP recorded at each monitoring point showed a rapid increase, which was related to the experience of the peak acceleration of ground shaking in that period. The final stage is 10.5s–15s, where the growth rate of the EPWP decreases significantly, levelling off and eventually approaching the peak.

Compare Fig. 16(a) and (b) and (c), the pore pressure oscillation of the soil around the pile is severe, which can easily cause shear dilation, especially in the range of  $0.63m (\approx 1D)$  where pile-soil interaction is significant, pore pressure changes are prominent; After exceeding the range of  $4.81m (\approx 7D)$ , the oscillation pore pressure is weak. Significant accumulation of EPWP in Far-pile soils, with peak  $R_u = 0.89$  and high degree of liquefaction (indicated by  $R_u \geq 0.8$ ).

Figs. 17–19 illustrate the complete process of the system at three cases. At 4 s–12 s, the affected domain around the pile is approximately a wedge-shaped region centered on the pile axis, with a length of  $14D$  and a depth of  $9D$  from the ground surface. At the mud level and mid-section

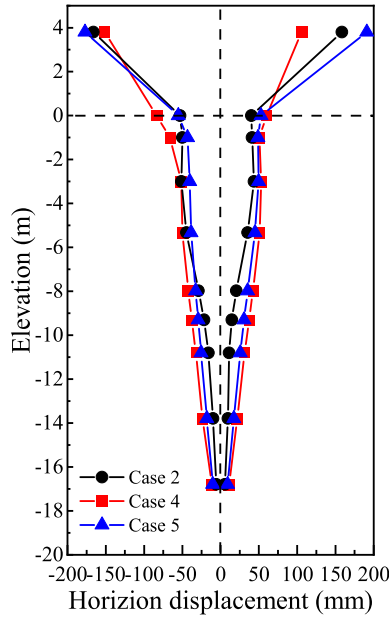


Fig. 21. Horizontal displacement envelope of the pile profile for three cases.

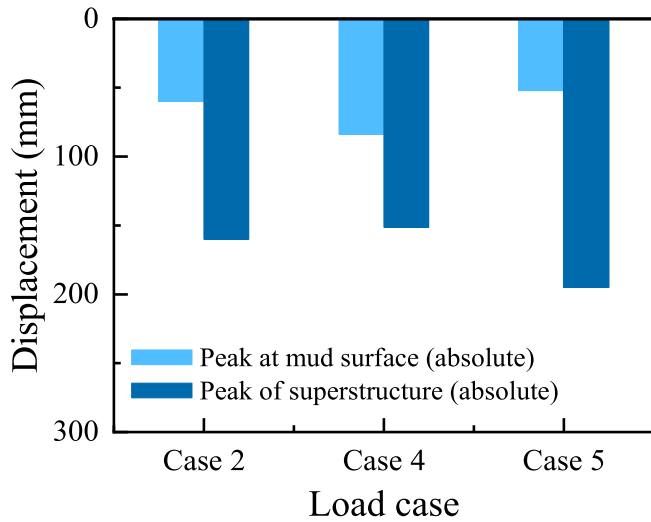


Fig. 22. Horizontal peak displacement of mud surface and pile top at different liquefaction depths.

of the pile body, the amplitude of EPWP oscillation is significant, with some parts of the soil experiencing transient  $R_u > 0.8$ ; At 12s–15s, the wedge-shaped affected area decreases, with liquefaction ( $R_u > 0.8$ ) first occurring in the middle of the sand layer, then progressing towards the top and away from the pile, ultimately resulting in liquefaction in most areas of the liquefiable loose sand ( $Dr = 55\%$ ), while the liquefied area of the non-liquefiable dense sand ( $Dr = 80\%$ ) is smaller, and the deep soil gradually transitions to a stable state.

The primary reasons for this phenomenon may be attributed to two points: Firstly, as the seismic acceleration diminishes, the interaction between the pile and the surrounding soil decreases, leading to a gradual reduction in the affected zone around the pile. Secondly, during an earthquake, the surface sand layer, due to its lower overburden stress, dissipates pore pressure more rapidly, whereas the middle and bottom sand layers drain upward more slowly, causing the sand to become increasingly compacted through vibration and leading to greater pore pressure accumulation, which results in progressive development towards the free field and the surface.

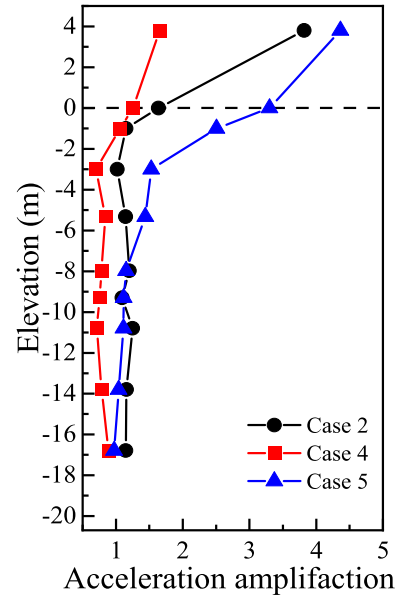


Fig. 23. Acceleration amplification factor envelope of the pile profile for three cases.

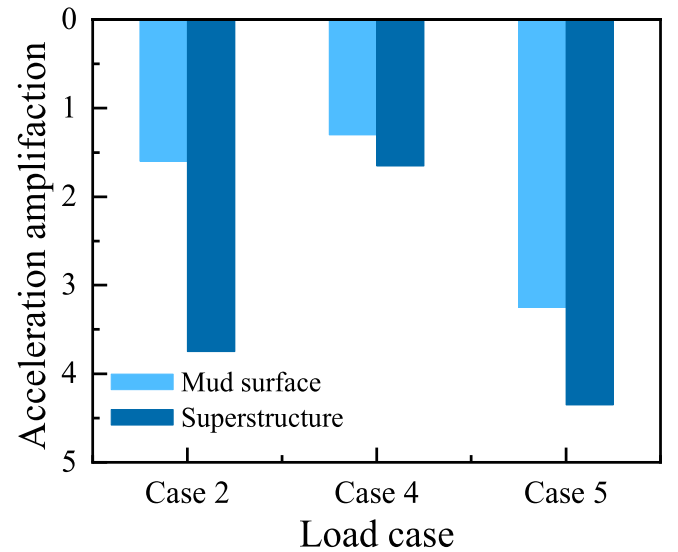


Fig. 24. Acceleration amplification coefficient of mud surface and superstructure of pile foundation with different liquefaction depth.

#### 4.2. Stress-strain response

Fig. 20 shows the shear stress-strain curves at four typical locations around the pile under three working cases. The figure clearly shows the transition of response mode from traditional hysteresis response (black line) to yield response (red line), which is due to the intensification of vibration and pore pressure, the final transition to the liquefied state is a small cyclic response (blue line).

Compare Fig. 20(b) and (c), it can be observed that in Case 4, the soil shear strain response at the mud surface location (A2) is smaller. This is due to the lower overburden stress on loose sand, resulting in a more pronounced liquefaction response of the soil and a weakened energy transfer to the superstructure, leading to weaker interaction forces between the mud surface and pile-soil system. The peak shear strain responses of the soil at mid-section locations (C2, E2) and pile end location (F2) in Case 4 are respectively 50 %, 21 %, and 47 % higher than those in Case 5 at corresponding positions. This is because loose sand has larger

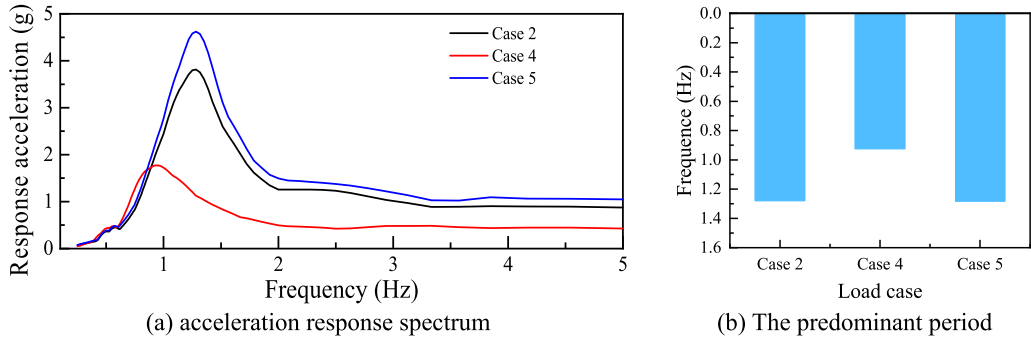


Fig. 25. Frequency response of superstructure with different liquefaction depth.

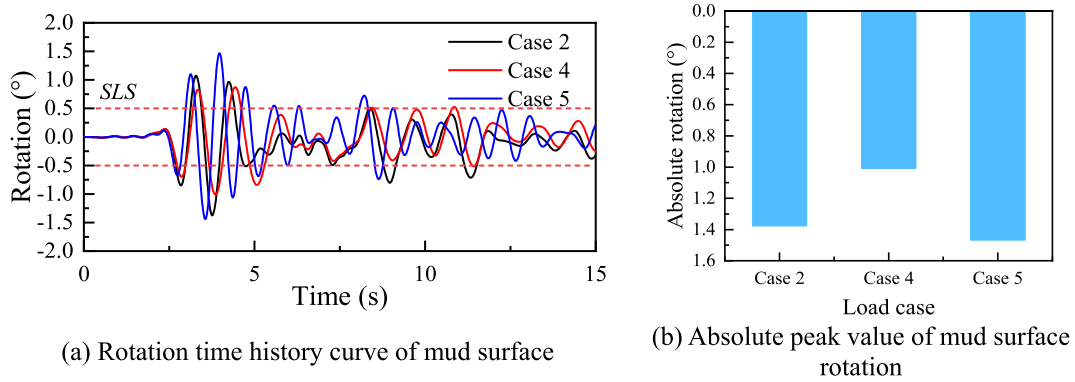


Fig. 26. Mud surface rotation response of pile foundation with different liquefaction depths.

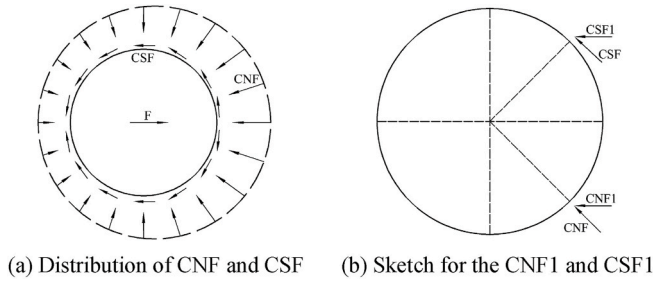


Fig. 27. Typical distribution of the calculated contact normal force (CNF) and contact shear force (CSF).

pores, which leads to rapid accumulation of excess pore water pressure during seismic shearing contraction, causing a decrease in soil stiffness and greater plastic deformation shear strain, resulting in a more significant liquefaction response. Fig. 20(a) further demonstrates that liquefaction reduces soil stiffness, leading to significant shear strain at the locations of loose sand around the pile (A2, C2).

#### 4.3. Horizontal displacement response

Fig. 21 displays the envelope curves of horizontal displacements for the pile foundation under three working cases. The horizontal displacement of the pile increases with decreasing depth and the displacement of the superstructure is the largest, which is due to the fact that the superstructure is mainly subjected to inertial forces. Case 4 peak horizontal displacements below the mud surface are greater than Case 5, but peak horizontal superstructure displacements are less than Case 5. Whereas in Case 2, the envelope curve of horizontal displacements in liquefiable sand is significantly larger than in non-liquefiable soil layers, which further suggests that the liquefaction of soils exacerbates the

inclination of the piles in the soils. In Case 5, due to the soil being non-liquefiable and having relatively higher stiffness, the pile foundation exhibits elastic properties, leading to a larger horizontal displacement of the superstructure. For further analysis of pile-soil deformation behavior, refer to Section 4.7.

From Fig. 22, it can be observed that Case 4 exhibits the highest peak horizontal displacement at the mudline, whereas Case 5 shows the greatest difference in horizontal displacement between the mudline and the superstructure. The results indicate that the liquefaction of the sands increases the horizontal displacement of the pile at the mudline and reduces the horizontal displacement of the superstructure.

#### 4.4. Acceleration response

Fig. 23 shows the acceleration amplification factor envelope of the pile profile. The acceleration amplification factor is defined as the ratio of the peak acceleration at the measurement point to the peak input acceleration at the base of the soil. Below 3 m, the acceleration response of the pile in Case 5 increases with decreasing depth, indicating a pronounced acceleration amplification effect. In contrast, the overall weakening of the acceleration response in Case 4 suggests that the liquefaction significantly reduced the pile's acceleration response. In Case 2, the acceleration response initially increases and then decreases. This variation is primarily attributed to the fact that in dense sand, the earthquake-induced vibrations enhance the soil's stiffness, facilitating the transfer of acceleration to the structure, whereas in loose sand, liquefaction causes significant dissipation of seismic energy within the soil foundation, thereby reducing the pile's acceleration response.

It is worth noting that at the junction of loose sand and dense sand ( $-9.3\text{m}$ ), the acceleration amplitude of the structure will suddenly decrease, indicating that the discontinuity of foundation materials affects the acceleration response of the pile body at the junction. Fig. 24 shows that the soil liquefaction response will reduce the acceleration response of pile foundation mud position and superstructure.

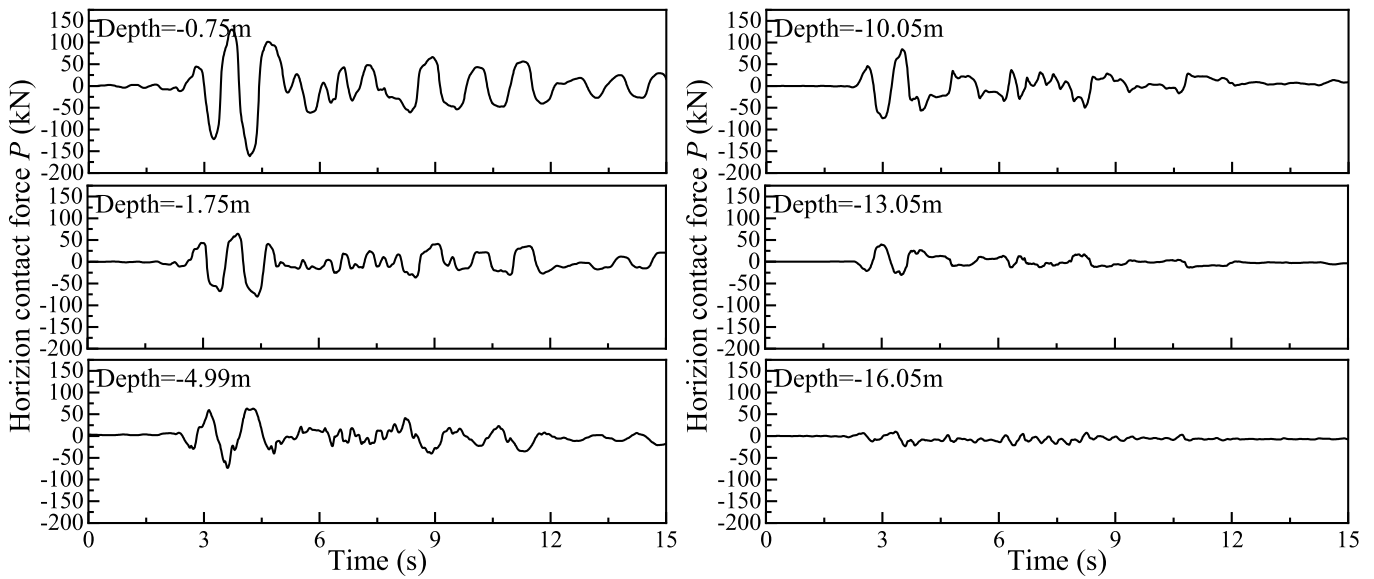


Fig. 28. Case 2 horizontal contact force time course curves at different elevations.

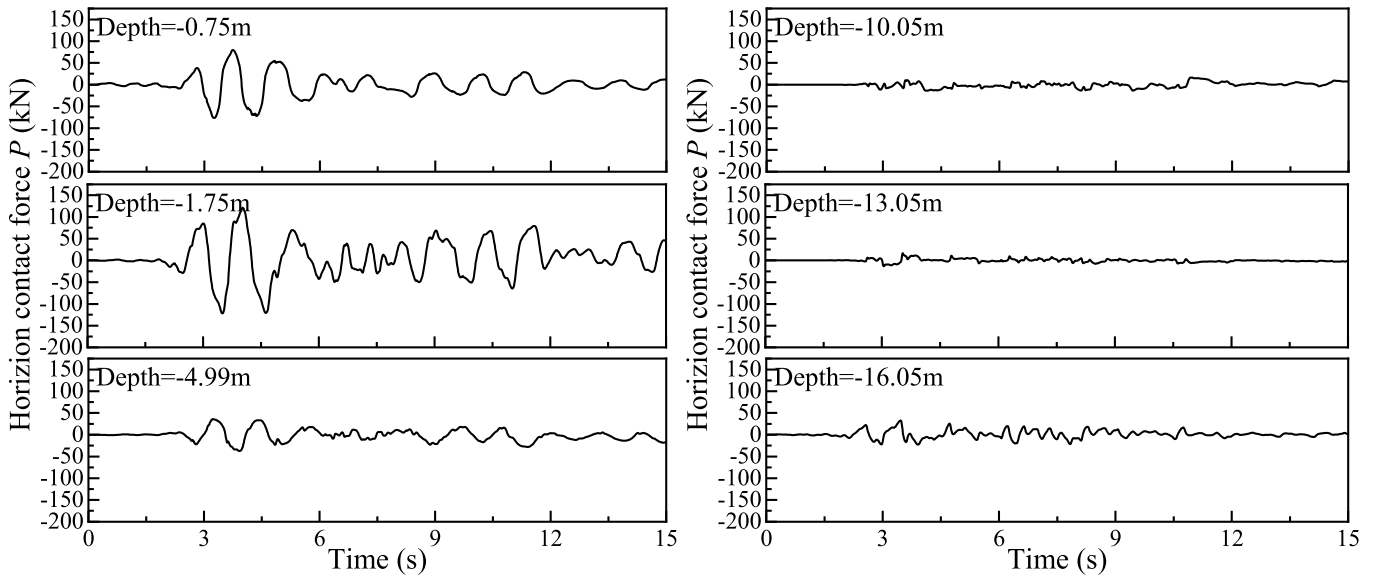


Fig. 29. Case 4 horizontal contact force time course curves at different elevations.

During the operation of an OWT, it is necessary to pay attention to the changes in its inherent frequencies, with the rotor's rotational frequency being 1P (1P refers to the frequency band between the lowest and highest speeds per minute, 0.1–0.2Hz). For a three-blade wind turbine, there is a shadowing effect as the blades pass in front of the tower, which occurs at a frequency of 3P (0.31–0.66Hz).

Fig. 25 illustrates that Case 4 exhibits the lowest structural frequency, while Case 2 and Case 5 show nearly identical frequencies. A comparison between Case 4 and Case 5 indicates that the liquefaction response of loose sand significantly reduces the natural frequency of the superstructure. In offshore wind engineering, as the frequency approaches the 3P frequency, the risk of structural resonance increases. Additionally, the structural frequency response decreases with increasing liquefiable depth. The reduction in structural frequency reflects the period elongation caused by soil softening, which is a prominent feature of soil–structure interaction effects. Unlike the equivalent linear analysis, the present model dynamically captures this behavior through a state-dependent constitutive relationship that governs the

stiffness degradation of liquefiable sands. However, the predominant seismic periods of Case 2 and Case 5 remain nearly the same (see Fig. 25 (b)), as both cases involve pile foundations embedded in non-liquefiable sand, where the pile tip is strongly constrained. This further confirms that liquefiable soil layers significantly influence the frequency response of the superstructure.

#### 4.5. Rotation response

The rotation of OWTs is a crucial factor affecting their operation, and Det Norske Veritas (DNV) recommends a maximum allowable rotation at mudline of  $0.5^\circ$  [87]. As depicted in Fig. 26, all operational conditions surpass the serviceability limit state (SLS), indicating the occurrence of tilting failure in pile foundations. Contrary to expectations, Case 4 exhibits the minimum rotation at mudline due to loose sand liquefaction, while Case 5 with dense sand experiences the highest amplitude and absolute peak values (see Fig. 26(b)). This discrepancy arises from the weakened energy transmission to the superstructure after loose sand



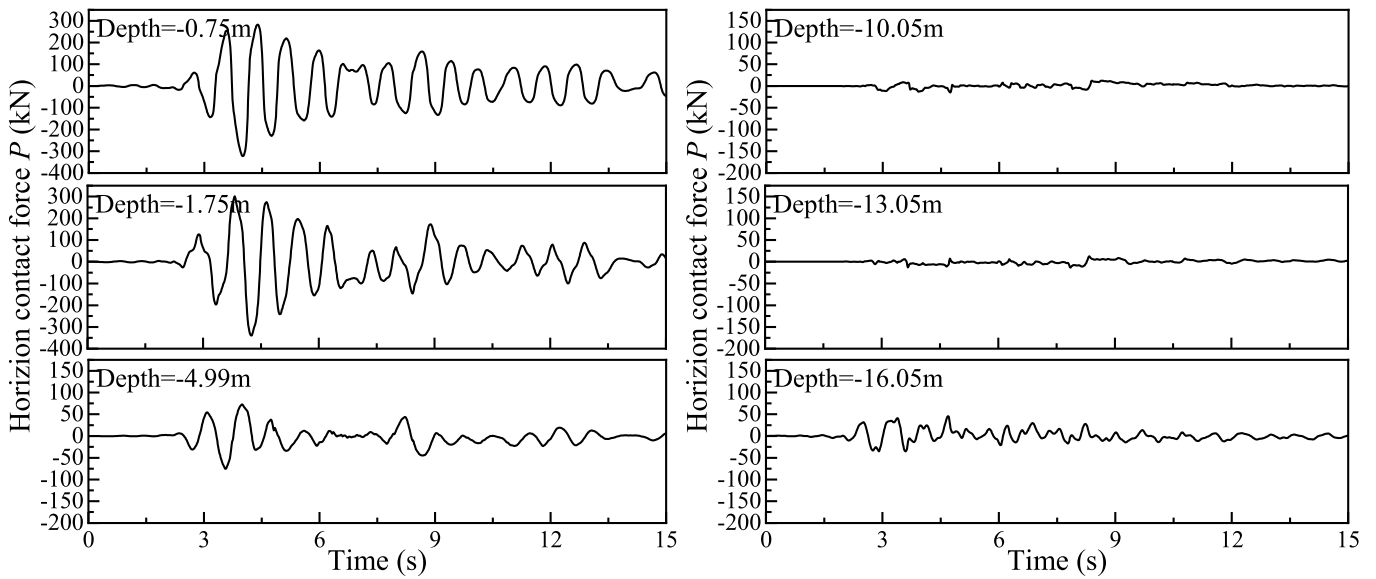


Fig. 30. Case 5 horizontal contact force time course curves at different elevations.

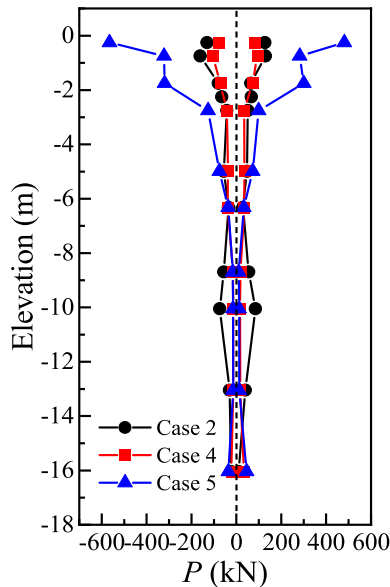


Fig. 31. Horizontal contact force envelope curves at different liquefaction depths.

liquefaction, resulting in reduced inertia forces and a relatively rigid pile foundation with smaller rotations. Conversely, dense sand demonstrates higher stiffness leading to greater inertia forces on the superstructure and consequently larger elastic amplitudes and rotations at mudline.

#### 4.6. Pile-soil interaction

By extracting the contact force on the contact surface unit, the horizontal contact force  $P$  at a certain depth is calculated to study the distribution pattern of pile-soil interaction. The typical distributions of circumferential normal force (CNF) and contact shear force (CSF) around the pile are shown in Fig. 27(a). Fig. 27(b) illustrates the x-component of CNF (CNF1) and CSF (CSF1) at a specific position on the cross-section of the pile.

The horizontal contact force  $P$  at a certain depth of the pile body can be determined by the sum of CNF1 and CSF1 around the pile, as shown

in the following equation:

$$P = \sum_{i=1}^n (CNF_1 + CSF_1) \quad (5)$$

where  $n$  is the number of interface elements outside the cross-section of the pile body at a certain depth. Figs. 28–30 present the development of horizontal contact forces at different elevations between the pile and soil under three working conditions. The results indicate that the horizontal contact force within the vertical influence zone (Depth = 9D) is significantly greater than in other areas, bearing a larger horizontal load capacity. As depth increases, the horizontal contact force gradually decreases, following a similar pattern observed in non-liquefiable soil layers.

Fig. 31 provides an envelope diagram of peak horizontal contact forces between piles and soil. In Case 2 and Case 4, due to pore pressure accumulation in the upper loose sand layer, the pile's horizontal bearing capacity is noticeably weakened, much lower than that in Case 5. Comparing Case 4 with Case 5, regardless of whether it is loose or dense sand, the pile within the vertical influence zone bears most of the main horizontal load capacity. The relationship between peak horizontal contact forces and soil depth is not entirely linear. Additionally, there is also a prominent level of lateral contact force at the interface between loose sand and dense sand in Case 2, indicating that material discontinuity affects load characteristics on pile-soil interfaces.

#### 4.7. Deformation mode

Fig. 32 presents three deformation patterns of pile foundations under three different working conditions. As mentioned earlier, after loose sand liquefaction (Case 4), the stiffness weakens and there is a larger horizontal displacement below the mud surface of the pile foundation. However, the inertia force of the superstructure is weaker, so the pile foundation above the mud surface exhibits relatively rigid behavior. The amplitude and accumulation of corner rotation at the mud surface are smaller.

Case 5, with relatively high relative stiffness of the dense sand, exerts strong constraints on the pile foundation below the mud surface, resulting in smaller horizontal displacement. However, the inertia forces of the superstructure are larger, causing elastic behavior in the pile foundation above the mud surface and leading to greater displacement and accumulation of angular amplitude ( $\theta$ ) at the mud surface.

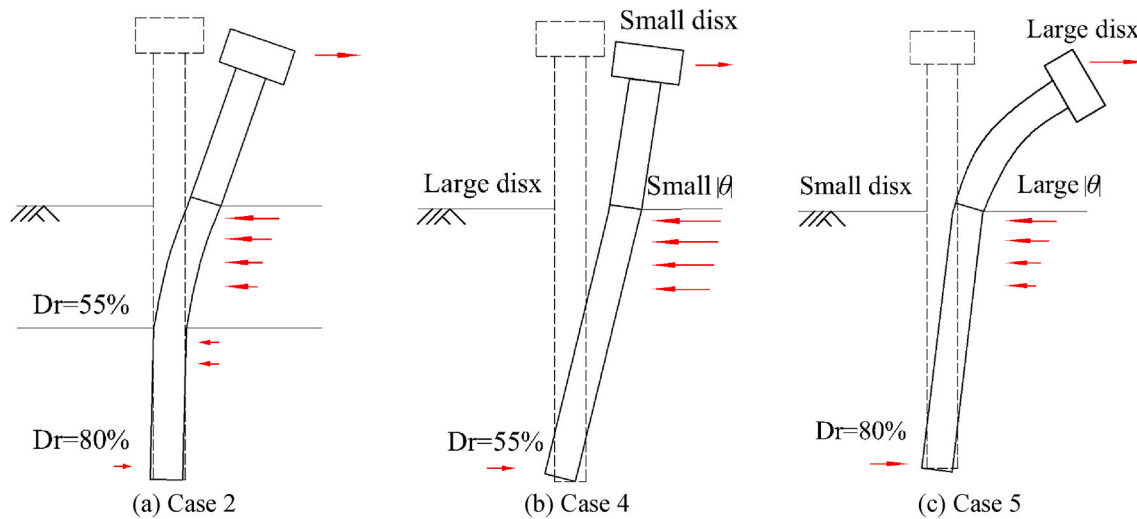


Fig. 32. Deformation patterns of pile foundations with different liquefaction depths.

In Case 2, the pile foundation combines the behavior of the previous two conditions. The embedding effect of the dense sand on the pile end in the lower layer results in minimal energy loss and still allows for transmission to the superstructure. Above the mud surface, both the pile foundation and structure exhibit rigid behavior, with displacements and rotations of the superstructure falling between those of the previous two cases. Due to their relatively rigid ends, pile foundations located in liquefiable sandy soil in the upper layer display more flexible behavior.

## 5. Research limitations in this work

The findings of this study offer new insights into the cross-scale dynamic response of superstructure-pile-soil systems in liquefiable sands. Compared with the conventional  $p$ - $y$  curve method and traditional FEM, the SBFEM-FEM coupling approach demonstrates significant advantages in both computational efficiency and accuracy, particularly in capturing the nonlinear interactions at the pile-soil interface. However, certain limitations remain:

- (1) Parameter dependency: The constitutive model parameters for sand used in this study were calibrated based on centrifuge test data from the literature. Future studies should incorporate in-situ test data to enhance the generalizability of the model parameters.
- (2) Geological complexity: The current model does not account for particle crushing under cyclic loading and is limited to horizontally layered sites and single-pile systems. Future work should extend the approach to multilayered soils and pile groups to better reflect practical engineering conditions.
- (3) Simplified assumptions in dynamic modeling: The numerical simulations based on the Wilson experiment did not incorporate equivalent linearization techniques, such as those accounting for period elongation and damping modification.

To address these limitations, future developments will focus on: (i) establishing machine learning-based parameter calibration methods to reduce reliance on traditional testing; (ii) extending the model framework to multilayered strata and pile group systems to explore liquefaction mechanisms under complex geological conditions; and (iii) incorporating a dedicated module for structural period estimation into the software. Specifically, Luco's improved Dunkerley approach [88] will be implemented to predict the fundamental period of the structure-foundation system, thereby enhancing its applicability in preliminary design [89,90].

## 6. Conclusions

This study integrates SBFEM theory with a generalized plastic constitutive model to develop a 3D cross-scale finite element analysis method for the foundation-pile system. The seismic response of single-pile foundations in liquefiable soil layers is investigated, with a detailed analysis of the spatiotemporal evolution of EPWP and pile deformation patterns. The key findings are as follows:

- (1) The proposed cross-scale discretization approach effectively reproduces centrifuge test results, accurately capturing the dynamic response of the structure and pore pressure evolution in the foundation soil. This method provides a reliable framework for large-scale prototype analysis of OWTs.
- (2) For loose sand layers, the soil at the shallow layer does not liquefy directly at the initial stage of the earthquake. Liquefaction first occurs in the middle of the loose sand layer and then spreads to the top and the far field, eventually covering the entire liquefiable soil layer.
- (3) A wedge-shaped influence zone forms around the pile at the mudline. Within this zone, pile-soil interaction and inertial forces induce an initial dilative response followed by contraction. Correspondingly, pore pressure first drops to negative values before accumulating positive excess pressure with significant oscillations. The pile foundation sustains substantial horizontal forces, whereas outside this zone, residual pore pressure remains high, and the horizontal forces on the pile are minimal.
- (4) While liquefaction intensifies pile inclination in loose sand layers, energy dissipation reduces the horizontal displacement and frequency of the superstructure, resulting in a smaller mudline rotation. In contrast, dense sand layers mitigate pile inclination; however, due to their higher relative stiffness, they amplify the acceleration and horizontal displacement response of the superstructure, leading to an increased mudline rotation.
- (5) The monopile exhibits three distinct deformation modes under varying liquefaction depths: In loose sand layers, the pile behaves as a rigid body as a whole; in dense sand layers, the region below the mudline remains rigid, while the portion above the mudline exhibits significant elastic characteristics; in stratified soils where the pile tip is embedded in dense sand, both ends of the pile remain rigid, whereas the middle section undergoes substantial flexible deformation.

## CRediT authorship contribution statement

**Degao Zou:** Writing – review & editing, Resources, Methodology, Funding acquisition, Conceptualization. **Tianju Wang:** Writing – original draft, Visualization, Validation, Software. **Jingmao Liu:** Validation, Methodology, Formal analysis. **Kai Chen:** Writing – original draft, Software, Project administration. **Bin Wang:** Resources, Investigation, Funding acquisition. **Xiuyang Zhang:** Visualization, Software.

## Declaration of competing interest

We would like to submit the enclosed manuscript entitled “High-fidelity numerical simulation of centrifuge tests on the superstructure-pile-liquefiable sand soil system”, which we wish to be considered for publication in *Soil Dynamics and Earthquake Engineering*. **We declare that we do not have any commercial or associative interest that represents a conflict of interest in connection with the work submitted.** The manuscript is approved by all authors for publication. The work described was original research that has not been published previously, and not under consideration for publication elsewhere, in whole or in part. All the authors listed have approved the manuscript that is enclosed.

## Acknowledgements

This work was supported by the National Natural Science Foundation of China (Grant Nos. 52109114, U2240211, and 52192674). The authors gratefully acknowledge the financial support and express their sincerest gratitude.

## Data availability

The data that has been used is confidential.

## References

- [1] De Risi R, Bhattacharya S, Goda K. Seismic performance assessment of monopile-supported offshore wind turbines using unscaled natural earthquake records. *Soil Dynam Earthq Eng* 2018;109:154–72.
- [2] De Groot MB, Bolton MD, Foray P, Meijers P, Palmer AC, Sandven R, Sawicki A, Teh TC. Physics of liquefaction phenomena around marine structures. *J Waterw Port Coast* 2006;132(4):227–43.
- [3] Ghosh B, Peiris N, Lubkowski Z. Assessment of seismic risk for the design of offshore structures in liquefiable soil. In: *Proceeding of 4th international conference on earthquake geotechnical engineering*; 2006.
- [4] Kaynia AM. Seismic considerations in design of offshore wind turbines. *Soil Dynam Earthq Eng* 2019;124:399–407.
- [5] Ashford SA, Boulanger RW, Donahue JL, Stewart JP, Harder Jr, L F, Kik. GEER reconnaissance reports. 2011.
- [6] Tsukamoto Y, Kawabe S, Kokusho T. Soil liquefaction observed at the lower stream of tonegawa river during the 2011 off the Pacific Coast of Tohoku earthquake. *Soils Found* 2012;52(5):987–99.
- [7] Amani S, Prabhakaran A, Bhattacharya S. Design of monopiles for offshore and nearshore wind turbines in seismically liquefiable soils: methodology and validation. *Soil Dynam Earthq Eng* 2022;157:107252.
- [8] Nikolaou S, Mylonakis G, Tazoh T. Kinematic pile bending during earthquakes: analysis and field measurements. *Geotechnique* 2001;51:425–40.
- [9] Sugimura Y, Karkee MB, Mitsuiji K. An investigation on aspects of damage to precast concrete piles due to the 1995 Hyogoken-Nambu earthquake. *Proceedings third UJNR workshop on soil-structure interaction*. 2004. p. 1–16. Menlo Park, California, USA.
- [10] Tokimatsu K, Tamura S, Suzuki H, Katsumata K. Building damage associated with geotechnical problems in the 2011 Tohoku Pacific Earthquake. *Soils Found* 2012;52(5):956–74.
- [11] Haskell JJM, Madabhushi G, Cubrinovski M, Winkley A. Lateral spreading-induced abutment rotation in the 2011 Christchurch earthquake: observations and analysis. *Geotechnique* 2013;63:1310–27.
- [12] Byrne B, Leblanc C, Housley G. Response of stiff piles to long term cyclic loading. *Geotechnique* 2010;60:79–90.
- [13] Wilson DJ. Soil-pile-superstructure interaction in liquefying sand and soft clay. Davis, USA: University of California; 1998. PhD Thesis.
- [14] Bhattacharya S, Madabhushi SPG, Bolton MD. An alternative mechanism of pile failure in liquefiable deposits during earthquakes. *Geotechnique* 2004;54(3):203–13.
- [15] Yu H, Zeng X, Li B, Lian J. Centrifuge modeling of offshore wind foundations under earthquake loading. *Soil Dynam Earthq Eng* 2015;77:402–15.
- [16] Wang X, Zeng X, Li X, Li J. Liquefaction characteristics of offshore wind turbine with hybrid monopile foundation via centrifuge modelling. *Renew Energy* 2020;145:2358–72.
- [17] Dou P, Xu C, Du X, Chen S. Influence of structure on the aseismic stability and dynamic responses of liquefiable soil. *Bull Earthq Eng* 2022;20:55–76.
- [18] Xu Y, Shen T, Zuo J, Bhattacharya S, Han Q. Shaking table tests and numerical analysis of monopile-supported offshore wind turbines under combined wind, wave and seismic loads. *Soil Dynam Earthq Eng* 2024;183:108793.
- [19] Song J, Yang Y, Jia K, Dou P, Ma X, Shen H. Seismic response and instability analysis of the liquefiable soil-piles-superstructure interaction system. *Structures* 2023;54:134–52.
- [20] Kim DH, Lee SG, Lee IK. Seismic fragility analysis of 5 MW offshore wind turbine. *Renew Energy* 2014;65:250–6.
- [21] Janalizadeh A, Zahmatkesh A. Lateral response of pile foundations in liquefiable soils. *J Rock Mech Geotech Eng* 2015;7(5):532–9.
- [22] Wang X, Ye A, Ji B. Fragility-based sensitivity analysis on the seismic performance of pile-group-supported bridges in liquefiable ground undergoing scour potentials. *Eng Struct* 2019;198:109427.
- [23] Patra SK, Haldar S. Seismic response of monopile supported offshore wind turbine in liquefiable soil. *Structures* 2021;31:248–65.
- [24] Patra SK, Haldar S. Seismic performance of multimegawatt offshore wind turbines in liquefiable soil under horizontal and vertical motions. *Int J GeoMech* 2022;22(3):04021305.
- [25] Yu Y, Chen X, Guo Z, Zhang J, Lü Q. Robust design of monopiles for offshore wind turbines considering uncertainties in dynamic loads and soil parameters. *Ocean Eng* 2022;266:112822.
- [26] Shi S, Zhai E, Xu C, Iqbal K, Sun Y, Wang S. Influence of pile-soil interaction on dynamic properties and response of offshore wind turbine with monopile foundation in sand site. *Appl Ocean Res* 2022;126:103279.
- [27] Brandenberg Scott J, Boulanger Ross W, Kutter Bruce L, Chang D. Static pushover analyses of pile groups in liquefied and laterally spreading ground in centrifuge tests. *J Geotech Geoenviron Eng* 2007;133(9):1055–66.
- [28] Liyanapathirana DS, Poulos HG. Pseudostatic approach for seismic analysis of piles in liquefying soil. *J Geotech Geoenviron Eng* 2005;131(12):1480–7.
- [29] Cubrinovski M, Kokusho T, Ishihara K. Interpretation from large-scale shake table tests on piles undergoing lateral spreading in liquefied soils. *Soil Dynam Earthq Eng* 2006;26(2):275–86.
- [30] Brandenberg Scott J, Zhao M, Boulanger Ross W, Wilson Daniel W. p-y plasticity model for nonlinear dynamic analysis of piles in liquefiable soil. *J Geotech Geoenviron Eng* 2013;139(8):1262–74.
- [31] Mu L, Chen W, Zhang Y, Chen X, Li W. A framework of analytical methods for horizontal behaviours of monopiles under V-H-M loads in sand. *Mar Georesour Geotechnol* 2022;40:349–60.
- [32] Mu L, Wang S, Huang M. Ultimate lateral resistance of single piles in sand. *IOP Conf Ser Earth Environ Sci* 2024;1336:012039.
- [33] Zhang X, Zhu D, Xu C, Du X. Research on p-y curves of soil-pile interaction in saturated sand foundation in weakened state. *Rock Soil Mech* 2020;41(7):2252–60.
- [34] Byrne BW, Burd HJ, Gavin KG, Housley GT, Jardine RJ, McAdam RA, Martin CM, Potts DM, Taborda DMG, Zdravkovic L. PISA: recent developments in offshore wind turbine monopile design. In: Randolph MF, Doan DH, Tang AM, Bui M, Dinh VN, editors. *Proceedings of the 1st Vietnam symposium on advances in offshore engineering, Energy and geotechnics*; 2019. p. 350–5.
- [35] Abdel-Rahman K, Achmus M. Finite element modelling of horizontally loaded monopile foundations for offshore wind energy converters in Germany. In: *Proceedings of the international symposium on frontiers in offshore geotechnics*; 2005. p. 391–6.
- [36] Choo Yun W, Kim D. Experimental development of the p-y relationship for large-diameter offshore monopiles in sands: centrifuge tests. *J Geotech Geoenviron Eng* 2016;142(1):04015058.
- [37] Cheng Z, Jeremić B. Numerical modeling and simulation of pile in liquefiable soil. *Soil Dynam Earthq Eng* 2009;29(11):1405–16.
- [38] Zhao HY, Jeng DS, Liao CC, Zhu JF. Three-dimensional modeling of wave-induced residual seabed response around a mono-pile foundation. *Coast Eng* 2017;128:1–21.
- [39] Hussein AF, El Naggar MH. Seismic axial behaviour of pile groups in non-liquefiable and liquefiable soils. *Soil Dynam Earthq Eng* 2021;149:106853.
- [40] Mo T, Wu Q, Li D, Du W. Influence of ground motion characteristics (velocity pulse and duration) on the pile responses in liquefiable soil deposits. *Soil Dynam Earthq Eng* 2022;159:107330.
- [41] Chen W, Jiang Y, Xu L, Liu C, Chen G, Wang P. Seismic response of hybrid pile-bucket foundation supported offshore wind turbines located in liquefiable soils. *Ocean Eng* 2023;269:113519.
- [42] Cheng X, Li Y, Mu K, El Naggar MH, Zhou Y, Wang P, Sun X, Liu J. Seismic response of tripod suction bucket foundation for offshore wind turbine in sands. *Soil Dynam Earthq Eng* 2024;177:108353.
- [43] Wang R, Fu P, Zhang J-M. Finite element model for piles in liquefiable ground. *Comput Geotech* 2016;72:1–14.
- [44] Esfah PK, Kaynia AM. Earthquake response of monopiles and caissons for Offshore Wind Turbines founded in liquefiable soil. *Soil Dynam Earthq Eng* 2020;136:106213.
- [45] Bao X, Wu S, Liu Z, Su D, Chen X. Study on the nonlinear behavior of soil-pile interaction in liquefiable soil using 3D numerical method. *Ocean Eng* 2022;258:111807.

- [46] Gao Z, Lu D, Hou Y, Li X. Constitutive modelling of fabric effect on sand liquefaction. *J Rock Mech Geotech Eng* 2023;15:926–36.
- [47] Shan Z, Zhu Z, Wang D, Ye G. Numerical modeling of the dynamic response of an elastoplastic seabed under wave-current interactions. *J Ocean Univ China* 2023;22: 43–52.
- [48] Lü X, Huang M, Andrade JE. Modeling the static liquefaction of unsaturated sand containing gas bubbles. *Soils Found* 2018;58:122–33.
- [49] Lü X, Xue D, Zhang B, Zhong Q. Experimental studies and constitutive modeling of static liquefaction instability in sand–clay mixtures. *Int J GeoMech* 2022;22: 04022149.
- [50] Liu H, Wang C, Ding X, Zhang Y. Comparative numerical analysis of the response of laterally loaded pile in coral and silica sands. *Acta Geotech* 2023;18:4767–87.
- [51] Zhang X, Lan H, Zhao X, Xu C, Jia K. Study on different reinforcement methods of inclined liquefiable site. *Soil Dynam Earthq Eng* 2024;176:108342.
- [52] Rahmani A, Pak A. Dynamic behavior of pile foundations under cyclic loading in liquefiable soils. *Comput Geotech* 2012;40:114–26.
- [53] Patra SK, Haldar S, Bhattacharya S. Predicting tilting of monopile supported wind turbines during seismic liquefaction. *Ocean Eng* 2022;252:111145.
- [54] Abbasi H, Binesh SM, El Naggar MH. Response analysis of single pile embedded in saturated sand under bidirectional cyclic loading. *Soil Dynam Earthq Eng* 2023; 166:107756.
- [55] Wang X, Wang W, Li J. Assessment on earthquake-induced liquefaction around a hybrid monopile foundation for offshore wind turbines with a transition layer model. *Ocean Eng* 2023;282:115028.
- [56] Wotherspoon LM. Three dimensional pile finite element modelling using OpenSees. NZSEE conference proceedings. Napier; 2006. 2006.
- [57] Sánchez M, Roeset JM. Evaluation of models for laterally loaded piles. *Comput Geotech* 2013;48:316–20.
- [58] Liu J, Zou D, Kong X. A two-mechanism soil–structure interface model for three-dimensional cyclic loading. *Int J Numer Anal Methods GeoMech* 2020;44(15): 2042–69.
- [59] Chen K, Zou D, Kong X, Yu X. An efficient nonlinear octree SBFEM and its application to complicated geotechnical structures. *Comput Geotech* 2018;96: 226–45.
- [60] Zou D, Teng X, Chen K, Yu X. An extended polygon scaled boundary finite element method for the nonlinear dynamic analysis of saturated soil. *Eng Anal Bound Elem* 2018;91:150–61.
- [61] Zou D, Teng X, Chen K, Liu J. A polyhedral scaled boundary finite element method for three-dimensional dynamic analysis of saturated porous media. *Eng Anal Bound Elem* 2019;101:343–59.
- [62] Zou D, Kong X, Liu J, et al. Theoretical introduction and user manual of the GEODYNA7.0 : a high-performance finite element analysis software system for large-scale geotechnical engineering. Dalian: Dalian University of Technology; 2022.
- [63] Zou D, Xu B, Kong X, Liu H, Zhou Y. Numerical simulation of the seismic response of the Zipingpu concrete face rockfill dam during the Wenchuan earthquake based on a generalized plasticity model. *Comput Geotech* 2013;49:111–22.
- [64] Gong J, Zou D, Kong X, Liu J, Chen K. A coupled meshless-SBFEM-FEM approach in simulating soil-structure interaction with cross-scale model. *Soil Dynam Earthq Eng* 2020;136:106214.
- [65] Gong J, Zou D, Kong X, Liu J, Qu Y. An approach for simulating the interaction between soil and discontinuous structure with mixed interpolation interface. *Eng Struct* 2021;237:112035.
- [66] Qu Y, Zou D, Chen K, Liu J. Three-dimensional refined analysis of seismic cracking and anti-seismic measures performance of concrete face slab in CFRDs. *Comput Geotech* 2021;139:104376.
- [67] Nie X, Chen K, Zou D, Kong X, Liu J, Qu Y. Slope stability analysis based on SBFEM and multistage polytree-based refinement algorithms. *Comput Geotech* 2022;149: 104861.
- [68] Chen K, Zou D, Liu J, Zhuo Y. A high-precision formula for mixed-order polygon elements based on SBFEM. *Comput Geotech* 2023;155:105209.
- [69] Liu J, Zou D, Ning F, Kong X. A unified constitutive model for instantaneous elastic-plastic and time-dependent creep behaviour of gravelly soils under complex loading. *Can Geotech J* 2023;60(11):1613–28.
- [70] Wang ZL, Dafalias Yannis F, Shen CK. Bounding surface hypoplasticity model for sand. *J Eng Mech* 1990;116(5):983–1001.
- [71] Li XS. A sand model with state-dependent dilatancy. *Geotechnique* 2002;52(3): 173–86.
- [72] Bardet J-P. Scaled memory description of hysteretic material behavior. *J Appl Mech* 1996;63.
- [73] Arulmoli K, Muralitharan K, Hossain M, Fruth L. VELACS (verification of liquefaction analyses by centrifuge studies) laboratory testing program: soil data report. 1992.
- [74] Chen K, Zou D, Tang H, Liu J, Zhuo Y. Scaled boundary polygon formula for cosserat continuum and its verification. *Eng Anal Bound Elem* 2021;126:136–50.
- [75] Xu X, Wang X, Yang H, Yang Z, He Y. Development of a three-dimensional multiscale octree SBFEM for viscoelastic problems of heterogeneous materials. *CMES-Comp Model Eng* 2024;(140):1831–61.
- [76] Chen K, Zou D, Yi G, Nie X, Qu Y. A flexible mixed-order formula for tetrahedron elements based on SBFEM. *Comput Geotech* 2024;171:106390.
- [77] Chen K, Zou D, Kong X, Chan A, Hu Z. A novel nonlinear solution for the polygon scaled boundary finite element method and its application to geotechnical structures. *Comput Geotech* 2017;82:201–10.
- [78] Song C, Wolf JP. The scaled boundary finite-element method—alias consistent infinitesimal finite-element cell method—for elastodynamics. *Comput Methods Appl Mech Eng* 1997;147:329–55.
- [79] Song C, Wolf JP. The scaled boundary finite element method—alias consistent infinitesimal finite-element cell method—for elastodynamics. *Comput Methods Appl Mech Eng* 1997;147:329–55.
- [80] Achmus M, Kuo YS, Abdel-Rahman K. Behavior of monopile foundations under cyclic lateral load. *Comput Geotech* 2009;36(5):725–35.
- [81] Li F, Han J, Lin C. Effect of scour on the behavior of laterally loaded single piles in marine clay. *Mar Georesour Geotechnol* 2013;31(3):271–89.
- [82] Page AM, Klinkvort RT, Bayton S, Zhang Y, Jostad HP. A procedure for predicting the permanent rotation of monopiles in sand supporting offshore wind turbines. *Mar Struct* 2021;75:102813.
- [83] Zhang X, Zou D, Liu J, Chen K, Li X, Wang T. A developed soil reaction model for large-diameter monopiles in sand based on hyperbolic curves. *Comput Geotech* 2024;172:106468.
- [84] Said ID, De Gennaro V, Frank R. Axisymmetric finite element analysis of pile loading tests. *Comput Geotech* 2009;36(1–2):6–19.
- [85] Madabhushi GSP, Knappett JA, Haigh SK. Design of pile foundations in liquefiable soils. Imperial College Press; 2010.
- [86] Beaty MH, Byrne PM. UBCSAND constitutive model version 904aR 2011. Itasca UDM Web Site 2011;69(3).
- [87] DNV (Det Norske Veritas). Support structures for wind turbines. DNVGL-ST-0126. Hovik, Denmark: DNV; 2021.
- [88] Luco J. Bounds for natural frequencies, Dunkerley's formula and application to soil–structure interaction. *Soil Dynam Earthq Eng* 2013;47:32–7.
- [89] Xiong W, Jiang L, Li Y. Influence of soil–structure interaction (structure-to-soil relative stiffness and mass ratio) on the fundamental period of buildings: experimental observation and analytical verification. *Bull Earthq Eng* 2016;14: 139–60.
- [90] Forcellini D. A 3-DOF system for preliminary assessments of the interaction between base isolation (BI) technique and soil structure interaction (SSI) effects for low-rise buildings. *Structures* 2024;59:105803.